

Coulomb screening and thermodynamic measurements in magic-angle twisted trilayer graphene

Xiaoxue Liu¹, Naiyuan James Zhang¹, K. Watanabe², T. Taniguchi², and J.I.A. Li^{1*}

¹*Department of Physics, Brown University, Providence, RI 02912, USA and*
²*National Institute for Materials Science, 1-1 Namiki, Tsukuba 305-0044, Japan*

(Dated: November 30, 2021)

The discovery of magic-angle twisted trilayer graphene (tTLG) adds a new twist to the family of graphene moiré. The additional graphene layer unlocks a series of intriguing properties in the superconducting phase, such as the violation of Pauli limit and re-entrant superconductivity at large in-plane magnetic field. In this work, we integrate magic-angle tTLG into a double-layer structure to study the superconducting phase. Utilizing proximity screening from the adjacent metallic layer, we examine the stability of the superconducting phase and demonstrate that Coulomb repulsion competes against the mechanism underlying Cooper pairing. Furthermore, we use a combination of transport and thermodynamic measurements to probe the isospin order, which points towards a spin-polarized and valley-unpolarized isospin configuration at half moiré filling, and for the nearby fermi surface. Our findings provide important constraints for theoretical models aiming to understand the nature of superconductivity. A possible scenario is that electron-phonon coupling stabilizes a superconducting phase with a spin-triplet, valley singlet order parameter.

Graphene moiré structures provide a paradigm system to study correlated physics and superconductivity in the 2D limit. A simple twist between graphene layers is shown unlock a rich phase space, where correlation driven insulators [1–3] coexist with superconductivity [4–6] and ferromagnetism [7–11]. As an important step towards a better microscopic understanding of the superconducting phase in graphene moiré, it is recently demonstrated that Cooper pairing in magic-angle twisted bilayer graphene (tBLG) competes against the influence of Coulomb repulsion between charge carriers [12–14], suggesting that superconductivity in the bilayer moiré likely arises from electron-phonon coupling. At the same time, a Pomeranchuk-type phase transition is observed in tBLG, where the high temperature phase is associated with the large electronic entropy and fluctuating isospin moments [15, 16]. The Pomeranchuk effect points towards small isospin stiffness in the moiré band of tBLG. These observations set the stage for the intriguing open questions regarding the nature of superconductivity in graphene moiré systems.

Superconductivity is recently reported in twisted tri-

layer graphene at the predicted magic angle, adding a new and intriguing member to graphene moiré structures. This three-layered structure is shown to be highly versatile, as band dispersion and Fermi surface contour are both suggested to be tunable with a perpendicular electric field D [17, 18]. Interestingly, the superconducting phase in magic-angle tTLG remains robust against a large in-plane magnetic field, which violates the Pauli limit for conventional spin-singlet superconductors [19]. This observation provides experimental support for spin-triplet pairing, where two electrons in a Cooper pair share the same spin quantum number. Such pairing symmetry has been previously observed in a range of unconventional superconductors, such as the Anderson-Brinkman-Morel phase of Helium-3 superfluid [20], Ru_2SO_4 [21] and UPt_3 [22, 23]. However, graphene moiré structures feature a spin-valley SU_4 symmetry, requiring us to consider both isospin flavors in order to determine the superconducting order parameter.

In this work, we examine two aspects of the superconducting phase in tTLG using a combination of Coulomb screening, thermodynamic and transport measurements. By controlling the strength of Coulomb interaction with proximity screening, we show that superconductivity becomes more robust when Coulomb repulsion is suppressed, suggesting that Coulomb repulsion competes against the mechanism underlying Cooper pairing, which is consistent with previous observations in magic-angle tBLG [12, 13]. In addition, we study thermodynamic properties of tTLG using a combination of transport and chemical potential measurements. The thermodynamic energy gap at half moiré fillings is shown to be insensitive to a large in-plane magnetic field, which is indicative of a spin-polarized and valley-unpolarized isospin configuration. Furthermore, we examine the phase boundary of the Pomeranchuk-type transition and show that the spin degree of freedom is frozen owing to large stiffness. As a result, valley isospin plays a dominating role in the Pomeranchuk-type phase transition. The large spin stiffness offers further support for the spin-polarized isospin order at half moiré filling. Since the superconducting phase is associated with the fermi surface reconstruction at half-moiré filling, identifying the isospin order of the underlying fermi surface provides constraints for the pairing symmetry of superconductivity.

The geometry of the double-layer structure is shown in Fig. 1a, where a Bernal bilayer graphene (BLG) is placed

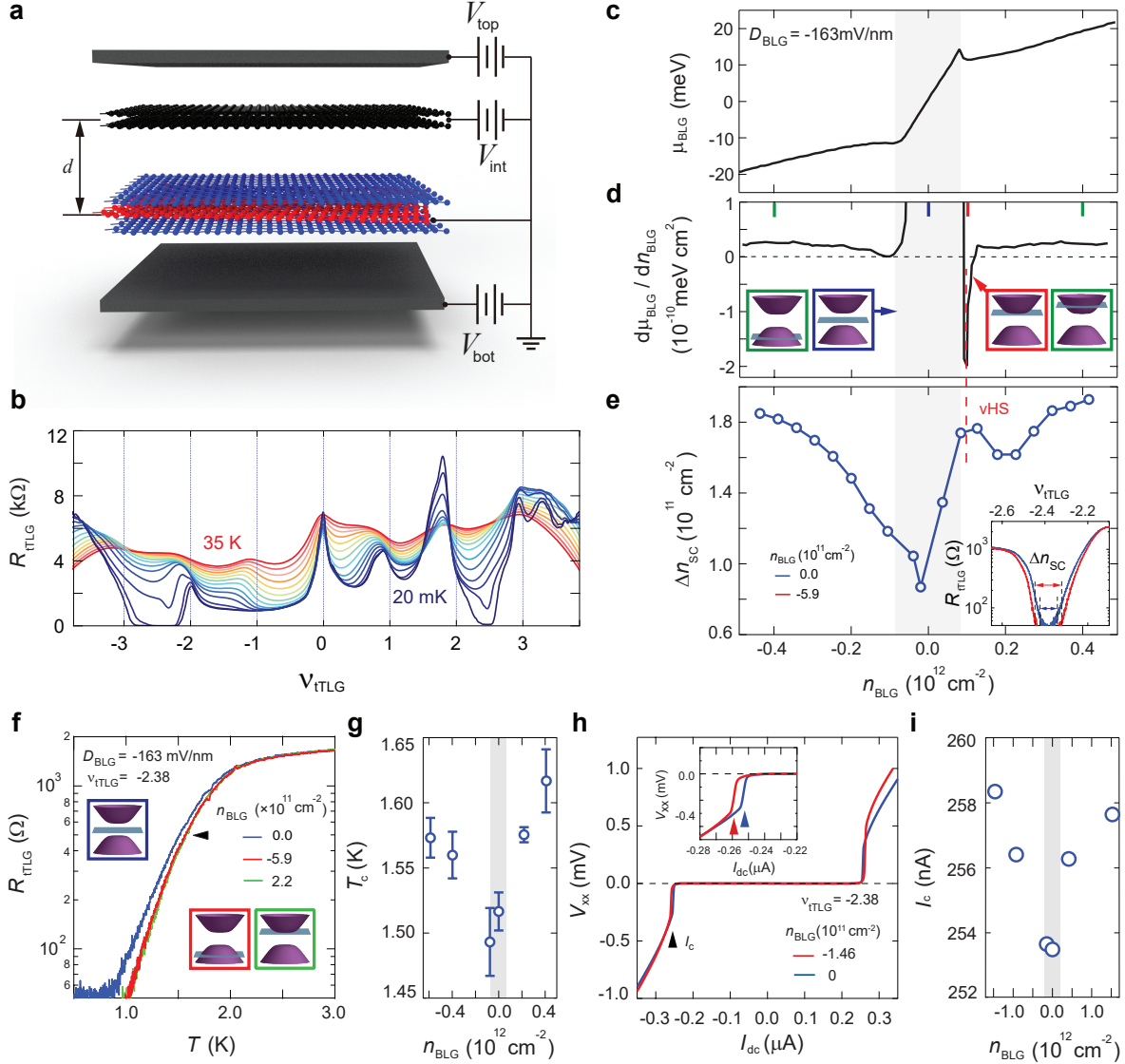


FIG. 1. Magic-angle tTLG in a double-layer structure and Coulomb screening. (a) Schematic of the hybrid double-layer structure consisting of a Bernal BLG and a magic-angle tTLG, separated by a thin insulating barrier with the thickness of $d = 2$ nm. (b) Longitudinal resistance measured from tTLG R_{tTLG} as a function of ν_{tTLG} at different temperature and $D_{BLG} = 0$ mV/nm. (c) Chemical potential μ_{BLG} and (d) inverse compressibility $d\mu_{BLG}/dn_{BLG}$ of BLG as a function of BLG density n_{BLG} at $T = 20$ mK. μ_{BLG} is extracted from longitudinal resistance R_{tTLG} measured as a function of V_{int} and V_{top} . Negative $d\mu_{BLG}/dn_{BLG}$ on the electron edge of the energy gap points toward large density of state associated with a van Hove singularity where screening is enhanced. (e) The density range of the superconducting region Δn_{SC} as a function of BLG density n_{BLG} at $T = 20$ mK. Inset: R_{tTLG} as a function of moiré filling ν_{tTLG} measured with different n_{BLG} at $T = 20$ mK and $D_{BLG} = -163$ mV/nm. Δn_{SC} is determined by the boundary of the superconducting region, which is defined by the density where R_{tTLG} increases above the noise level. (f) R_{tTLG} as a function of temperature T measured at different n_{BLG} and $D_{BLG} = -163$ mV/nm. The transition temperature T_c is operationally defined as 30% of extrapolated normal state resistance, marked by the black arrow. (g) T_c as a function of n_{BLG} measured at $D_{BLG} = -163$ mV/nm. At the optimal doping, $D_{BLG} = -163$ mV/nm and $n_{BLG} = 0$ correspond to $D_{tTLG} = 95$ mV/nm for tTLG (see Fig. S3 and S9). (h) $V_{xx} - I$ curves of the superconducting phase measured at $D_{BLG} = 125$ mV/nm, $T = 20$ mK and different n_{BLG} . Critical current I_c is defined by the onset in the $V_{xx} - I$ curves, where the sample transitions from superconducting to normal state behavior. (i) Critical current I_c as a function of n_{BLG} at $D_{BLG} = 125$ mV/nm, where tTLG experiences $D_{tTLG} = 390$ mV/nm at the optimal doping and $n_{BLG} = 0$. (f-i) Measurements are all performed at the optimal doping of the superconducting phase in tTLG at $\nu_{tTLG} = -2.38$ (see Fig. S16) [24]. While tTLG is tuned to the optimal doping, in (e), (g) and (i), D_{tTLG} varies by than ~ 10 mV/nm over the density range of n_{BLG} . The shaded stripes highlight the density range where BLG is insulating.

in proximity with tTLG, separated by an insulating barrier of hexagonal boron nitride (hBN). By applying voltage bias on top and bottom graphite gate electrodes, V_{top} and V_{bot} , as well as across the insulating hBN barrier, V_{int} , we are able to independently control carrier density in BLG and tTLG, n_{BLG} and n_{tTLG} , along with the displacement field D . Transport measurement in tTLG reveals a series of correlated states appearing at commensurate fillings, which are evidenced by resistance peaks in longitudinal resistance, resets in Hall density, extra Landau fans and the sawtooth pattern in chemical potential and electronic compressibility [4–6, 12]. At the same time, superconductivity emerges as carrier density is detuned from the CI at $\nu_{tTLG} = 2 + \delta$ and $-2 - \delta$ [17, 18]. We note that commensurate fillings are determined based on the combination of quantum oscillation and chemical potential measurement (see Fig. S15 and Fig. 2). Based on the carrier density at commensurate fillings, we obtain a twist angle of 1.5° . Notably, transport behavior from different parts of the sample suggests that twist angle variation across different parts of the sample is on the order of $\pm 0.01^\circ$ (Fig. S1). The excellent sample homogeneity, combined with the double-layer structure, allows us to study the moiré band of tTLG using Coulomb screening and thermodynamic measurements.

First, we utilize Coulomb screening to investigate the role of Coulomb repulsion in stabilizing the superconducting phase. Since Coulomb screening from BLG is determined by its electronic compressibility, its strength can be characterized by mapping the position of the CNP in tTLG, which allows us to extract the chemical potential μ_{BLG} (Fig. 1c) and inverse compressibility $d\mu_{BLG}/dn_{BLG}$ (Fig. 1d) of BLG as a function of carrier density in BLG n_{BLG} [25]. According to Fig. 1c-d, large contrast in screening can be achieved by tuning n_{BLG} in the presence of a D -induced energy gap [12]. When the Fermi surface is inside the energy gap at the CNP, which is highlighted by the gray shaded area in Fig. 1c-e, BLG is highly incompressible. In this scenario, screening is absent and Coulomb repulsion within tTLG is maximized. On the other hand, BLG becomes compressible with increasing density n_{BLG} and Coulomb repulsion in tTLG is suppressed by screening. As the strength of screening varies with n_{BLG} , the stability of the superconducting phase, which is characterized by the density range of the superconducting region Δn_{SC} , changes accordingly. Here we define the boundaries of the superconducting region as the density where R_{tTLG} increases above the noise level (inset of Fig. 1e) [12]. Δn_{SC} is at a minimum when BLG is fully incompressible, whereas it increases with increasing n_{BLG} (Fig. 1e). Notably, Δn_{SC} exhibits a local maximum near the electron-edge of the energy gap, which coincides with enhanced screening at the van Hove singularity in BLG (Fig. 1d).

The effect of controlling Coulomb screening is also observed in the critical temperature T_c and critical current

I_c of the superconducting phase at the optimal doping (See Fig. S16). Both T_c and I_c confirm the same trend as shown in Fig. 1e. The transition temperature T_c , operationally defined as 30% of extrapolated normal state resistance, increases from ~ 1.5 K at $n_{BLG} = 0$ to ~ 1.6 K when BLG is compressible at large n_{BLG} (Fig. 1f-g). The percentage change in T_c of $\sim 7\%$ is in line with the effect of Coulomb screening observed in magic-angle tBLG [12]. The normal state resistance at $T \gtrsim 2K$ is shown to be insensitive to changes in the electronic compressibility of BLG (Fig. 1f), demonstrating that changes in impurity scattering does not play a dominating role in the stability of superconductivity [26]. In addition, the influence of tuning screening onsets near the downturn in the $R-T$ curve, which is characteristic of the emergence of Cooper pairing, suggesting that Coulomb screening is directly influencing the superconducting energy gap. The $I-V$ characteristics exhibits a similar, albeit less prominent response to variation in Coulomb repulsion: I_c increases as Coulomb repulsion is suppressed by tuning BLG from insulating to metallic (Fig. 1h-i).

In all three measurements shown in Fig. 1, the superconducting phase becomes more robust as BLG becomes metallic regardless of charge carrier polarity in BLG. Although varying n_{BLG} introduces small variations in the displacement field experienced by tTLG, D_{tTLG} , the robustness of the superconducting phase in all three measurements in Fig. 1 varies monotonically with D_{tTLG} (see Fig. S3 and S9). Combined with the fact that D_{tTLG} varies monotonically as a function of n_{BLG} , according to the capacitance model, the non-monotonic n_{BLG} -dependence on Coulomb screening response cannot be accounted for by the influence of varying D_{tTLG} . Taken together, we draw the conclusion that the stability of the superconducting phase anti-correlates with the strength of Coulomb repulsion in tTLG, which is consistent with the scenario where Cooper pair formation arises from a mechanism that competes against Coulomb repulsion, such as phonon-mediated coupling [12, 27–29].

Notably, the superconducting phase near $\nu_{tTLG} = \pm 2$ remains robust against a large in-plane magnetic field that exceeds the Pauli limit (Fig. 2a-b). The Pauli paramagnetic limit is defined as $B_{\parallel}^{Pauli} = 1.86 [\text{T/K}] \times T_c$ (take $g = 2$), where T_c is the critical temperature at $B = 0$ T [19]. This behavior is consistent with the Pauli limit violation in the previous observation [19], pointing towards an order parameter that is spin-triplet and potentially unconventional. It is worth pointing out that in the B -field range that exceeds the Pauli limit, the effect of Coulomb screening remains the same as $B = 0$, offering further confirmation that the mechanism underlying Cooper pairing competes against Coulomb repulsion (see Fig. S11) [24]. However, we note that such pairing mechanism does not offer definitive identification for the superconducting order parameter. To better understand the superconducting phase in tTLG, we will turn

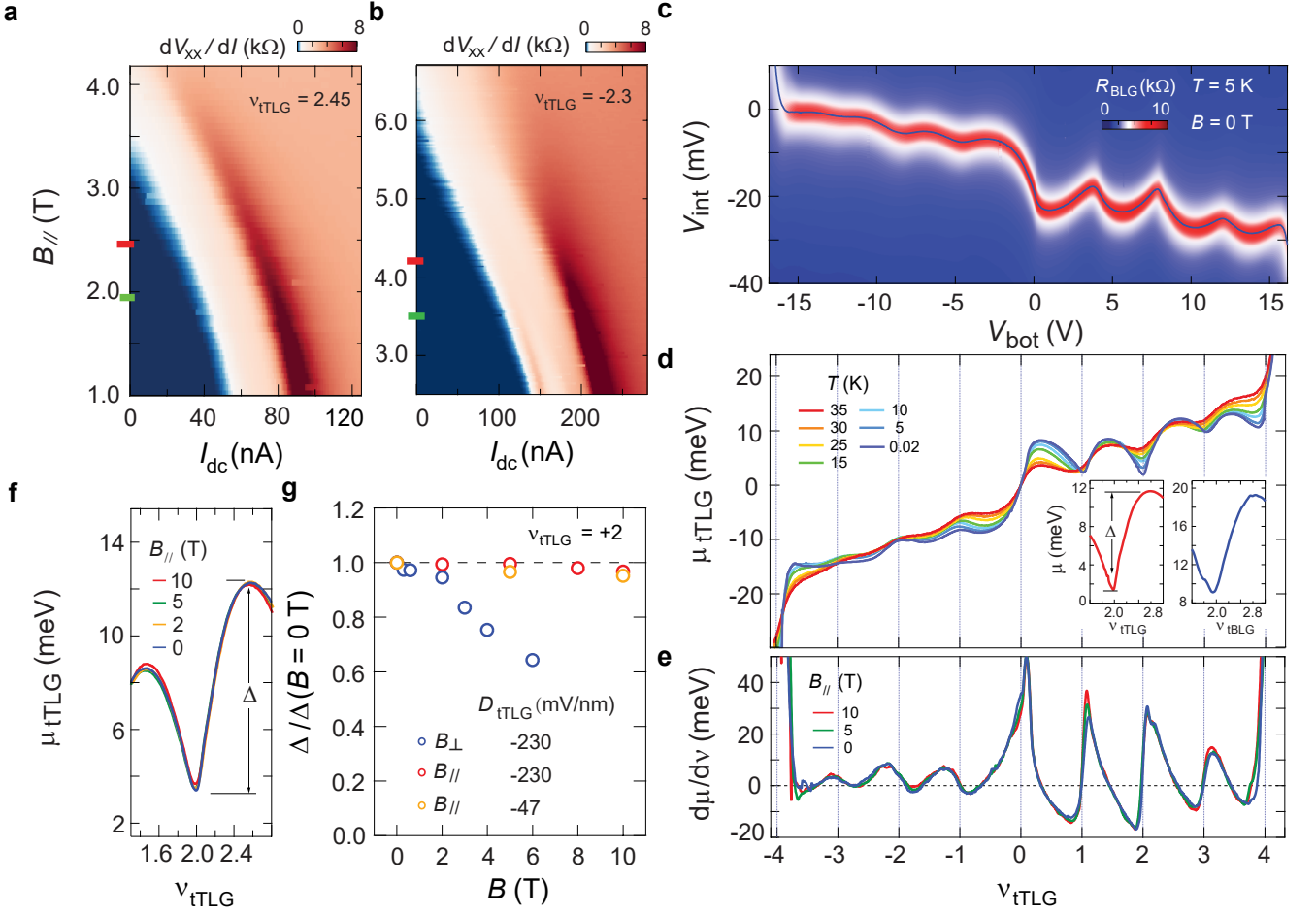


FIG. 2. **Isospin orders.** (a-b) Differential resistance dV_{xx}/dI as a function of in-plane magnetic field $B_{||}$ measured at (a) $\nu_{tTLG} = 2.45$ ($D_{tTLG} = -305$ mV/nm) and (b) -2.3 ($D_{tTLG} = 255$ mV/nm). The red and green horizontal lines mark the Pauli limit determined from the superconducting transition temperature T_c at $B = 0$ T, which are defined as 50% and 10% of extrapolated normal state resistance, respectively. (c) Longitudinal resistance R_{BLG} measured from Bernal BLG as a function of V_{int} and V_{bot} . Bernal BLG remains gapless at $D_{BLG} = 0$ throughout the measurement by keeping V_{top} zero. The blue solid curve tracks the CNP of Bernal BLG. (d-e) Chemical potential μ_{tTLG} at different temperatures, inverse compressibility $d\mu/d\nu$ at different in-plane magnetic field as a function of moiré filling ν_{tTLG} . Inset in (d): comparison of chemical potential near $\nu = +2$ measured from tTLG and tBLG using the same method at $T = 20$ mK. Results from this tBLG sample are also reported in [12] and [15]. The jump in the chemical potential is 10.3 meV for tTLG, and 10.2 meV for tBLG. (f) Chemical potential near $\nu_{tTLG} = +2$ at different in-plane magnetic field measured at $T = 5$ K and $D_{tTLG} = -230$ mV/nm. (g) Energy gap value, extracted from the jump in μ_{tTLG} , as a function of the in-plane and out-of plane magnetic field for different D_{tTLG} (see Fig. S12 for more details).

our attention to examine thermodynamic properties and the isospin order in the moiré flat band.

The double-layer structure allows us to directly extract the chemical potential of tTLG μ_{tTLG} based on the location of the charge neutrality point in BLG, which reflects the screening of electric field from the bottom gate electrode [25, 30]. Figure 2c-e plots μ_{tTLG} and its derivative, inverse compressibility $d\mu/d\nu$, as a function of moiré filling across the flat energy band. The net increase of μ_{tTLG} across the moiré band provides a direct measurement of the moiré bandwidth, which is less than 30 meV (Fig. 2d). The measured bandwidth for tTLG is much smaller than

tBLG (40 meV- 60 meV) [15, 30] and appears consistent with the calculation for tTLG based on the Bistritzer-Macdonald model [31, 32]. Between each commensurate filling, μ_{tTLG} exhibits a decreasing trend that stems from a strong exchange interaction and translates into a negative compressibility of the electron system [25, 33]. A smaller band width suggests that Coulomb interaction plays a more prominent role in tTLG, which is consistent with the fact that negative compressibility is observed throughout the moiré band. The series of peaks in $d\mu/d\nu$ at each commensurate filling correspond to Fermi surface reconstruction owing to a cascade of isospin-symmetry-

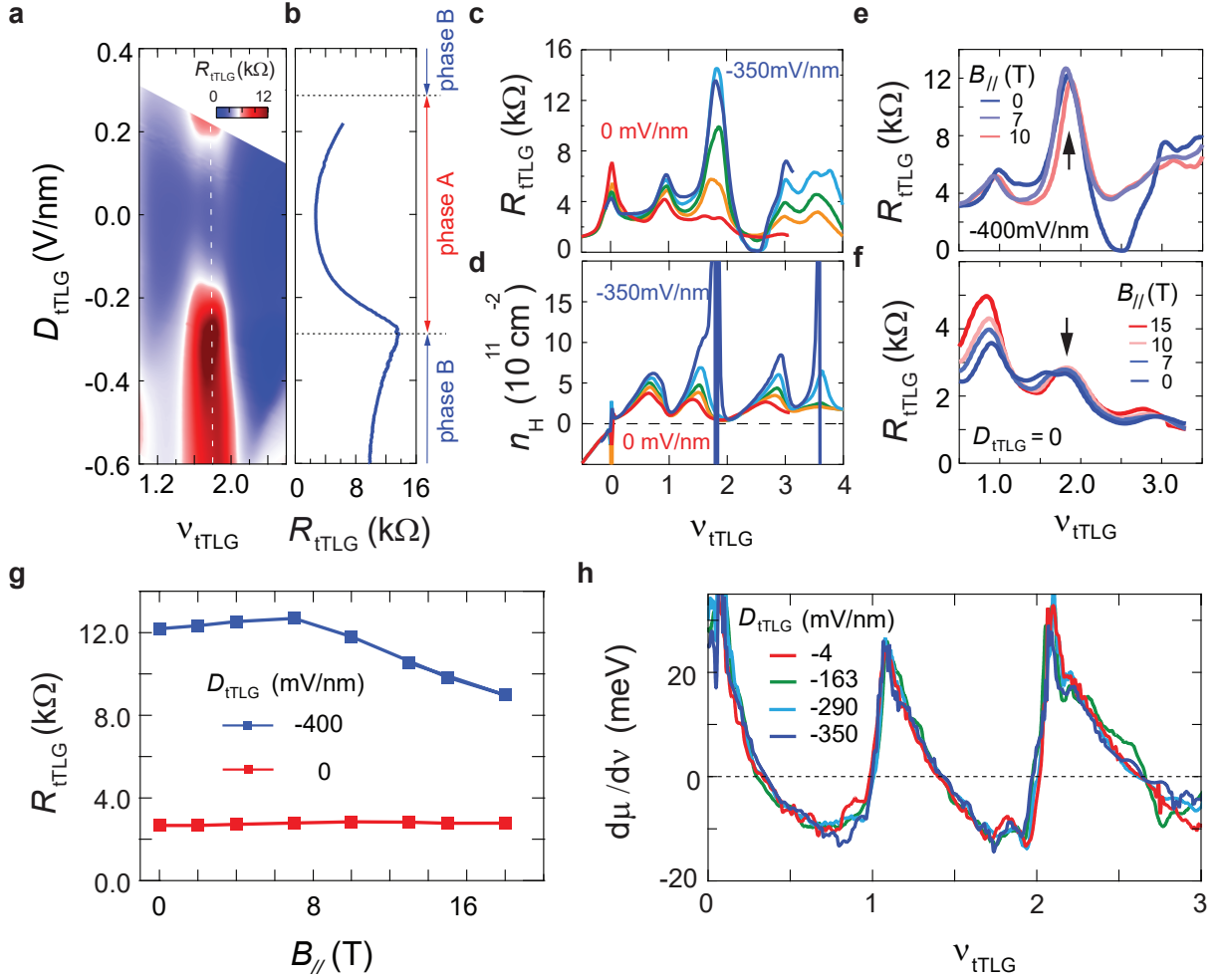


FIG. 3. **The effect of displacement field D_{tTLG} .** (a) Longitudinal resistance in tTLG, R_{tTLG} , as a function of moiré filling ν_{tTLG} and displacement field D_{tTLG} at $T = 20$ mK. (b) R_{tTLG} as a function of D_{tTLG} measured along the white vertical dashed line in (a). The value of resistance peak reveals two different transport behaviors at half-filling: the resistance peak is suppressed near $D = 0$, whereas a prominent peak emerges at large $|D_{tTLG}| > 200$ mV/nm. (c) Longitudinal resistance R_{tTLG} , (d) Hall density n_H as a function of ν_{tTLG} at $D_{tTLG} = 0, -163, -220, -290$ and -350 mV/nm measured at $T = 20$ mK. (e-f) Longitudinal resistance R_{tTLG} as a function of ν_{tTLG} at different in-plane magnetic field $B_{||}$ and $T = 300$ mK, measured at (e) $D_{tTLG} = -400$ mV/nm and (f) $D_{tTLG} = 0$. (g) The value of the resistance peak near half-filling marked by the black arrow in (e) and (f) as a function of $B_{||}$ at $T = 300$ mK. (h) Inverse compressibility $d\mu/d\nu$ measured from tTLG at different D_{tTLG} and $T = 20$ mK. D_{tTLG} in (h) is calculated at $\nu_{tTLG} = +2$.

breaking transitions (Fig. 2e) [30, 34–36]. It is worth pointing out that the behavior of μ_{tTLG} and $d\mu/d\nu$ of our sample shows an abundance of similarities with that of magic-angle twisted bilayer graphene [15, 16, 30], and the transport response exhibits excellent agreement with previous observation in magic-angle tTLG [17–19]. This indicates that our sample likely has the A-tw-A stacking order [37, 38].

The ability to probe μ_{tTLG} allows us to directly examine the isospin order of the fermi surface underlying the superconducting phase at $\nu_{tTLG} = 2 + \delta$ and $-2 - \delta$. This can be achieved by probing the robustness of correlation-driven insulating (CI) state at $\nu_{tTLG} = \pm 2$ as a func-

tion of in-plane magnetic field $B_{||}$. The jump in μ_{tTLG} near the half-filling corresponds to the thermodynamic energy gap of the CI $\Delta_{n_s/2}$ (Fig. 2f). Notably, $\Delta_{n_s/2}$ is insensitive to in-plane Zeeman coupling up to $B_{||} \sim 10$ T (Fig. 2g), whereas an out-of-plane B up to 6 T suppresses $\Delta_{n_s/2}$ by $\sim 40\%$. In comparison, $\Delta_{n_s/2}$ in tBLG exhibits a reduction of 12% to 75% at $B_{||} = 9$ T, depending on the measurement methods [5, 15]. Since the spin index couples to both in-plane and out-of-plane B and the valley index is only sensitive to out-of-plane Zeeman coupling, the distinct responses to different B -alignments point towards a spin-polarized, valley-unpolarized isospin configuration for $\nu_{tTLG} = +2$.

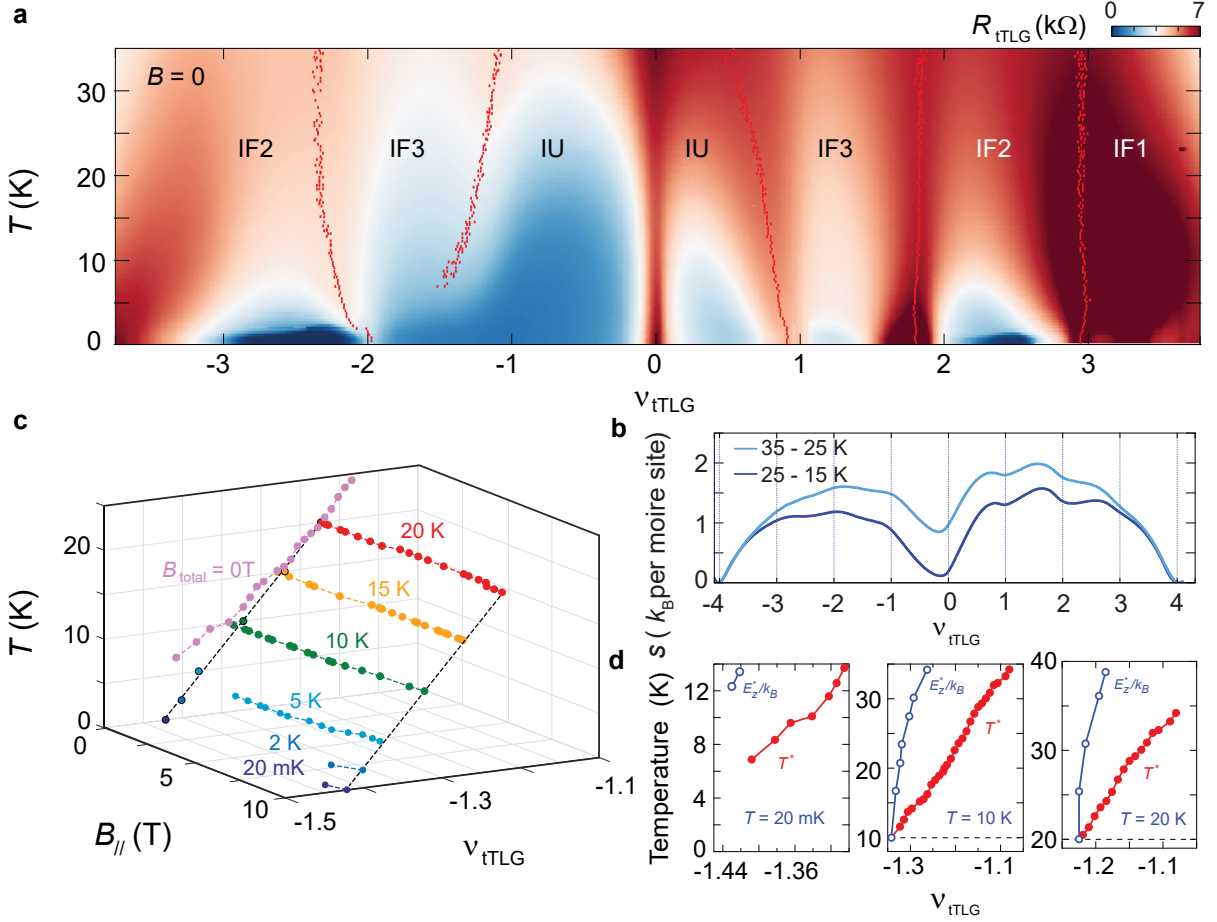


FIG. 4. **Isospin Pomeranchuk effect and spin stiffness.** (a) Longitudinal resistance R_{tTLG} measured from tTLG as a function of ν_{tTLG} and T at $D_{BLG} = 0$ mV/nm. Red circles mark the location of local maxima in R_{tTLG} showing phase boundaries between symmetry-breaking isospin ferromagnets (IF1, IF2, and IF3) and an isospin-unpolarized state (IU) [15]. (b) Electronic entropy, in units of k_B per moiré unit cell, as a function of moiré filling ν_{tTLG} at two different temperatures. Entropy is derived from the finite difference between $\mu(\nu_{tTLG})$ data measured at 15, 25 and 35 K. Entropy derivative $(\partial S/\partial \nu)_T$ is obtained based on the Maxwell relation $(\partial \mu/\partial T)_\nu = -(\partial S/\partial \nu)_T$, approximating $(\partial \mu/\partial T)_\nu$ from the finite difference of μ measured at two temperatures. Entropy per moiré unit cell is derived by integrating $(\partial S/\partial \nu)_T$ over ν . (c) The position of resistive peaks as a function of $B_{||}$ and T . The black solid circles represent peak position at $B_{||} = 10$ T, which are projected to the $B = 0$ plane. Dashed curves are polynomial fits to the dots at $B_{||} = 10$ T. (d) Phase boundaries for Zeeman-tuned transition (E_z^*/k_B , open blue circles) and temperature tuned transitions (T^* , solid red circles). Boundaries are shown as extracted both from R_{tTLG} peaks. An offset in Zeeman-tuned transitions are included to account for the temperature of the measurement.

To further confirm the isospin order at half-filled moiré band, we examine the transport behavior. Figure 3a-d show that varying D_{tTLG} has dramatic effect on both longitudinal resistance and Hall density near $\nu_{tTLG} = 2$ [17, 18]. The longitudinal resistance R_{tTLG} exhibits a distinguished peak at $\nu_{tTLG} = +2$ and large displacement field $|D_{tTLG}| > 200$, whereas the peak is suppressed at $D_{tTLG} = 0$. At the same time, a van Hove singularity emerges in the large $|D_{tTLG}|$ regime, evidenced by the diverging Hall density n_H near $\nu_{tTLG} = +2$ (Fig. 3d). Notably, the in-plane B dependence of the resistance peak over the entire D_{tTLG} range is consistent with the behavior of the thermodynamic energy gap. In the large D_{tTLG} regime, the resistance peak becomes slightly more

resistive up to $B_{||} \sim 7$ T before diminishing slightly at 10 T (Fig. 3e), whereas the peak value around $D_{tTLG} = 0$ remains unchanged up to $B_{||} = 15$ T (Fig. 3f). The in-plane B -dependence of the resistance peak further confirms the spin polarized and valley unpolarized isospin order at half-filled moiré band. If the superconducting phase inherits the isospin order of the underlying fermi surface, a natural order parameter is the spin-triplet, valley singlet [39, 40]. Such an order parameter is expected to remain robust against an in-plane B -field that exceeds the Pauli limit. We note that valley index couples to an in-plane magnetic field through a weak orbital effect [39], which could account for the weak $B_{||}$ dependence displayed by $\Delta_{n_s/2}$ (Fig. 2g) and the resistance peak

at $B_{\parallel} > 10$ T (Fig. 3g). At the same time, the orbital effect provides a pair breaking mechanism that destabilizes the superconductivity at large B_{\parallel} .

It is worth pointing out that varying D_{tTLG} has little influence on the thermodynamic gap (Fig. 2g) and electronic compressibility (Fig. 3h) at $\nu_{tTLG} = +2$. Figure 3h shows that both the location and amplitude of $d\mu/d\nu$ peaks remain the same over a wide range of D_{tTLG} . The lack of D_{tTLG} -dependence in electron compressibility, combined with the emergence of van Hove singularity near $\nu_{tTLG} = +2$ suggests that isospin-symmetry-breaking transitions are not influenced by the emergence of saddle-points in the Fermi surface [17, 18]. In addition, the distinct transport response and the robust energy gap in different D_{tTLG} regimes are indicative of different ground states at half moiré filling, tunable with D_{tTLG} . For example, a recent theoretical work proposed that the ground state at half-filled moiré band in tTLG transitions from an intervalley coherent semimetal around $D_{tTLG} = 0$ to a sublattice polarized insulator at large D_{tTLG} , which agrees well with our observations [41].

Lastly, we will characterize a more universal isospin property, spin stiffness, by examining the Pomeranchuk effect in tTLG. Figure 4a plots longitudinal resistance R_{tTLG} in the temperature-moiré filling ($T - \nu_{tTLG}$) map. Separated by resistive peaks in R_{tTLG} , different areas in the $T - \nu_{tTLG}$ map correspond to distinct isospin configurations, which are identified based on the degeneracy of quantum oscillations associated with each commensurate filling (see Fig. S15). As such, the phase boundary near $\nu_{tTLG} = -1$ marks a temperature driven phase transition from an iso-spin unpolarized (IU) state at low temperature to an iso-spin polarized (IF₃) state at high temperature. Such a transition can also be induced at low temperature by applying a large in-plane magnetic field B_{\parallel} , as an extra step in Hall density emerges at $B_{\parallel} = 10$ T (Fig. S4). The duality between the temperature-tuned and Zeeman-tuned transitions between the IU and IF₃ phases points towards a Pomeranchuk-type mechanism [15, 16]. In this scenario, the high temperature IF₃ phase is entropically favored compared to the IU phase owing to fluctuations in local isospin ferromagnetic moments. Notably, the electronic entropy s is extracted based on the temperature dependence of μ_{tTLG} and the Maxwell relation (Fig. 4b). s exhibits a robust minimum around the CNP, rises with both electron or hole doping, reaching a maximum of around $s/k_B \sim 1.5$ between $\nu_{tTLG} = 1$ and 2 before dropping back to zero at $\nu_{tTLG} = \pm 4$. The behavior of s , are in line with previous observations in tBLG [15, 16], highlighting that isospin fluctuations in these two graphene moiré systems are similar.

Notably, the effect of in-plane Zeeman coupling on the Pomeranchuk transition is much weaker in tTLG. By defining the transition based on the peak position in lon-

gitudinal resistance R_{tTLG} , we mark the phase boundary between the IU and IF₃ phases in the $T - B_{\parallel} - \nu_{tTLG}$ space (Fig. 4c). Figure 4c shows that the IU-IF₃ phase boundary is mostly insensitive to varying in-plane field up to $B_{\parallel} = 10$ T, even though it is highly tunable with increasing temperature. The effect of thermal and in-plane Zeeman energy, T^* and E_z^*/k_B , is quantitatively characterized in Fig. 4d. By comparing thermal and Zeeman energies associated with the same amount of shift in the IU-IF₃ boundary, $\Delta\nu^*$, we estimate the in-plane Zeeman coupling strength in tTLG to be at least four to eight times weaker compared to thermal effect. This is in stark contrast with previous observation in magic-angle tBLG, where temperature and Zeeman coupling are shown to have similar influence on the IU-IF₃ transition [15]. The weak in-plane Zeeman coupling points towards large spin stiffness, since the spin degree of freedom in tTLG is mostly frozen. As a result, the contribution of valley isospin plays a dominating role in the fluctuating isospin moments at high temperature and the associated electronic entropy.

Similar behavior is observed for the isospin transition near $\nu_{tTLG} = +1$ (Fig. S5), which can be directly compared with previous observations in magic-angle tBLG [4, 5, 16]. A Pomeranchuk-type mechanism is demonstrated by the Fermi surface reconstruction, evidenced by the jump in μ_{tTLG} and the sharp peak in $d\mu/d\nu$, which shifts to smaller filling with increasing temperature. At the same time, the position of the same isospin transition appears largely insensitive to in-plane Zeeman coupling, confirming that the spin degrees of freedom is frozen owing to large spin stiffness. Large spin stiffness in tTLG increases the energy cost to form spin skyrmions, making valley skyrmions energetically more favorable. In the scenario where superconductivity originates from topological textures [42], pairing between valley skyrmions is expected to play a more dominating role compared to spin skyrmions. We anticipate our findings will stimulate future investigations into the isospin order in tTLG and its role in the superconducting order parameter.

ACKNOWLEDGMENTS

We thank Andrea Young, Oskar Vafek and Yahui Zhang for helpful discussions. This work was primarily supported by Brown University. A portion of this work was performed at the National High Magnetic Field Laboratory, which is supported by the National Science Foundation Cooperative Agreement No. DMR-1644779 and the state of Florida. Device fabrication was performed in the Institute for Molecular and Nanoscale Innovation at Brown University. The authors acknowledge the use of equipment funded by the MRI award DMR-1827453. K.W. and T.T. acknowledge support from the EMEXT Element Strategy Initiative to Form Core Re-

search Center, Grant Number JPMXP0112101001 and the CREST(JPMJCR15F3), JST.

COMPETING FINANCIAL INTERESTS

The authors declare no competing financial interests.

* jia.li@brown.edu

- [1] X. Liu, Z. Hao, E. Khalaf, J. Y. Lee, Y. Ronen, H. Yoo, D. H. Najafabadi, K. Watanabe, T. Taniguchi, A. Vishwanath, *et al.*, *Nature* **583**, 221 (2020).
- [2] Y. Cao, D. Rodan-Legrain, O. Rubies-Bigorda, J. M. Park, K. Watanabe, T. Taniguchi, and P. Jarillo-Herrero, *Nature* **583**, 215 (2020).
- [3] Y. Cao, V. Fatemi, A. Demir, S. Fang, S. L. Tomarken, J. Y. Luo, J. D. Sanchez-Yamagishi, K. Watanabe, T. Taniguchi, E. Kaxiras, R. C. Ashoori, and P. Jarillo-Herrero, *Nature* **556**, 80 (2018).
- [4] Y. Cao, V. Fatemi, S. Fang, K. Watanabe, T. Taniguchi, E. Kaxiras, and P. Jarillo-Herrero, *Nature* **556**, 43 (2018).
- [5] M. Yankowitz, S. Chen, H. Polshyn, Y. Zhang, K. Watanabe, T. Taniguchi, D. Graf, A. F. Young, and C. R. Dean, *Science* **363**, 1059 (2019).
- [6] X. Lu, P. Stepanov, W. Yang, M. Xie, M. A. Aamir, I. Das, C. Urgell, K. Watanabe, T. Taniguchi, G. Zhang, A. Bachtold, A. H. MacDonald, and D. K. Efetov, arXiv preprint arXiv:1903.06513 (2019).
- [7] A. L. Sharpe, E. J. Fox, A. W. Barnard, J. Finney, K. Watanabe, T. Taniguchi, M. Kastner, and D. Goldhaber-Gordon, arXiv preprint arXiv:1901.03520 (2019).
- [8] M. Serlin, C. Tschirhart, H. Polshyn, Y. Zhang, J. Zhu, K. Watanabe, T. Taniguchi, L. Balents, and A. Young, arXiv preprint arXiv:1907.00261 (2019).
- [9] H. Polshyn, J. Zhu, M. Kumar, Y. Zhang, F. Yang, C. Tschirhart, M. Serlin, K. Watanabe, T. Taniguchi, A. MacDonald, and A. F. Young, *Nature* **588**, 66 (2020).
- [10] G. Chen, A. L. Sharpe, E. J. Fox, Y.-H. Zhang, S. Wang, L. Jiang, B. Lyu, H. Li, K. Watanabe, T. Taniguchi, *et al.*, *Nature* **579**, 56 (2020).
- [11] S. Chen, M. He, Y.-H. Zhang, V. Hsieh, Z. Fei, K. Watanabe, T. Taniguchi, D. H. Cobden, X. Xu, C. R. Dean, and M. Yankowitz, *Nature Physics* **17**, 374 (2021).
- [12] X. Liu, Z. Wang, K. Watanabe, T. Taniguchi, O. Vafek, and J. Li, *Science* **371**, 1261 (2021).
- [13] P. Stepanov, I. Das, X. Lu, A. Fahimniya, K. Watanabe, T. Taniguchi, F. H. Koppens, J. Lischner, L. Levitov, and D. K. Efetov, *Nature* **583**, 375 (2020).
- [14] Y. Saito, J. Ge, K. Watanabe, T. Taniguchi, and A. F. Young, *Nature Physics* **16**, 926 (2020).
- [15] Y. Saito, F. Yang, J. Ge, X. Liu, T. Taniguchi, K. Watanabe, J. Li, E. Berg, and A. F. Young, *Nature* **592**, 220 (2021).
- [16] A. Rozen, J. M. Park, U. Zondiner, Y. Cao, D. Rodan-Legrain, T. Taniguchi, K. Watanabe, Y. Oreg, A. Stern, E. Berg, *et al.*, *Nature* **592**, 214 (2021).
- [17] J. M. Park, Y. Cao, K. Watanabe, T. Taniguchi, and P. Jarillo-Herrero, *Nature* **590**, 249 (2021).
- [18] Z. Hao, A. Zimmerman, P. Ledwith, E. Khalaf, D. H. Najafabadi, K. Watanabe, T. Taniguchi, A. Vishwanath, and P. Kim, *Science* **371**, 1133 (2021).
- [19] Y. Cao, J. M. Park, K. Watanabe, T. Taniguchi, and P. Jarillo-Herrero, *Nature* **595**, 526 (2021).
- [20] D. Vollhardt and P. Wölfle, *The Superfluid Phases of Helium 3* (Taylor and Francis, 1990).
- [21] A. P. Mackenzie and Y. Maeno, *Reviews of Modern Physics* **75**, 657 (2003).
- [22] E. Schemm, W. Gannon, C. Wishne, W. Halperin, and A. Kapitulnik, *Science* **345**, 190 (2014).
- [23] J. Strand, D. Bahr, D. J. Van Harlingen, J. Davis, W. Gannon, and W. P. Halperin, *Science* **328**, 1368 (2010).
- [24] Please see the supplementary materials.
- [25] K. Lee, B. Fallahazad, J. Xue, D. C. Dillen, K. Kim, T. Taniguchi, K. Watanabe, and E. Tutuc, *Science* **345**, 58 (2014).
- [26] L. Ponomarenko, A. Geim, A. Zhukov, R. Jalil, S. Morozov, K. Novoselov, I. Grigorieva, E. Hill, V. Cheianov, V. Fal'ko, *et al.*, *Nature Physics* **7**, 958 (2011).
- [27] M. Ochi, M. Koshino, and K. Kuroki, *Phys. Rev. B* **98**, 081102 (2018).
- [28] B. Lian, Z. Wang, and B. A. Bernevig, *Phys. Rev. Lett.* **122**, 257002 (2019).
- [29] F. Wu, A. H. MacDonald, and I. Martin, *Phys. Rev. Lett.* **121**, 257001 (2018).
- [30] J. M. Park, Y. Cao, K. Watanabe, T. Taniguchi, and P. Jarillo-Herrero, *Nature* **592**, 43 (2021).
- [31] E. Khalaf, A. J. Kruchkov, G. Tarnopolsky, and A. Vishwanath, *Phys. Rev. B* **100**, 085109 (2019).
- [32] R. Bistritzer and A. H. MacDonald, *Proceedings of the National Academy of Sciences* **108**, 12233 (2011).
- [33] J. P. Eisenstein, L. N. Pfeiffer, and K. W. West, *Phys. Rev. B* **50**, 1760 (1994).
- [34] J. Kang, B. A. Bernevig, and O. Vafek, arXiv preprint arXiv:2104.01145 (2021).
- [35] U. Zondiner, A. Rozen, D. Rodan-Legrain, Y. Cao, R. Queiroz, T. Taniguchi, K. Watanabe, Y. Oreg, F. von Oppen, A. Stern, *et al.*, *Nature* **582**, 203 (2020).
- [36] D. Wong, K. P. Nuckolls, M. Oh, B. Lian, Y. Xie, S. Jeon, K. Watanabe, T. Taniguchi, B. A. Bernevig, and A. Yazdani, *Nature* **582**, 198 (2020).
- [37] H. Kim, Y. Choi, C. Lewandowski, A. Thomson, Y. Zhang, R. Polski, K. Watanabe, T. Taniguchi, J. Alicea, and S. Nadj-Perge, arXiv:2109.12127 (2021).
- [38] S. Turkel, J. Swann, Z. Zhu, M. Christos, K. Watanabe, T. Taniguchi, S. Sachdev, M. S. Scheurer, E. Kaxiras, C. R. Dean, and A. N. Pasupathy, arXiv:2109.12631 (2021).
- [39] J. Y. Lee, E. Khalaf, S. Liu, X. Liu, Z. Hao, P. Kim, and A. Vishwanath, *Nature communications* **10**, 1 (2019).
- [40] E. Cornfeld, M. S. Rudner, and E. Berg, *Physical Review Research* **3**, 013051 (2021).
- [41] M. Christos, S. Sachdev, and M. S. Scheurer, arXiv preprint arXiv:2106.02063 (2021).
- [42] E. Khalaf, S. Chatterjee, N. Bultinck, M. P. Zaletel, and A. Vishwanath, *Science advances* **7**, eabf5299 (2021).

SUPPLEMENTARY MATERIALS

Coulomb screening and thermodynamic measurements in magic-angle twisted trilayer graphene

Xiaoxue Liu, Naiyuan James Zhang, K. Watanabe, T. Taniguchi, J.I.A. Li[†]

[†] Corresponding author. Email: jia.li@brown.edu

I. Device Fabrication

The hybrid double-layer structure used in this study is fabricated by using the “cut-and-stack” and dry-transfer technique [12]. We cut a single monolayer graphene flake into three pieces by AFM before stacking. A poly(bisphenol A carbonate) (PC)/polydimethylsiloxane (PDMS) stamp mounted on a glass slide is used to pick up each layer sequentially. From top to bottom, the sequence of the stacking is: graphite as top gate electrode, 30 nm thick hBN as top dielectric, Bernal bilayer graphene, 2 nm thick hBN as the insulating barrier, magic-angle tTLG, 50 nm thick hBN as bottom dielectric, graphite as bottom gate electrode. The entire structure is released onto a Si/SiO₂ substrate. The hybrid double-layer stack is shaped into an aligned Hall bar geometry, as shown in Fig. S1a. In this geometry, electrical contacts to both Bernal bilayer and tTLG are made independently by the reactive ion etching of CHF₃/O₂ and deposition of the Cr/Au (2/100 nm) metal edge contacts, which enables the independent electrical measurements in tTLG and Bernal bilayer graphene.

To determine the carrier density associated with accurate integer filling, we use two independent methods in this work: (i) integer filling can be identified by extrapolating quantum oscillations associated with fermi surface reconstruction to $B = 0$; (ii) track the sawtooth pattern in chemical potential as a function of density. First, we use the quantum oscillations emanating from the charge neutral point and $\nu_{tTLG} = \pm 2$ to identify the location of the charge neutrality point and the carrier density at half moiré filling, n ($\nu_{tTLG} = \pm 2$). Assuming the density at full filling is twice that of half-filling, n ($\nu_{tTLG} = \pm 4$) = 2* n ($\nu_{tTLG} = \pm 2$), we calculate the twisted angle θ based on this equation: $n(\nu_{tTLG} = \pm 4) = 8\theta^2/\sqrt{3}a^2$, where $a = 0.246$ nm is the lattice constant of graphene. Secondly, we double check this calculation by comparing with the sawtooth pattern in chemical potential as a function of carrier densities in tTLG, which confirms a twist angle of 1.5 degrees with an error bar of 0.01 degree.

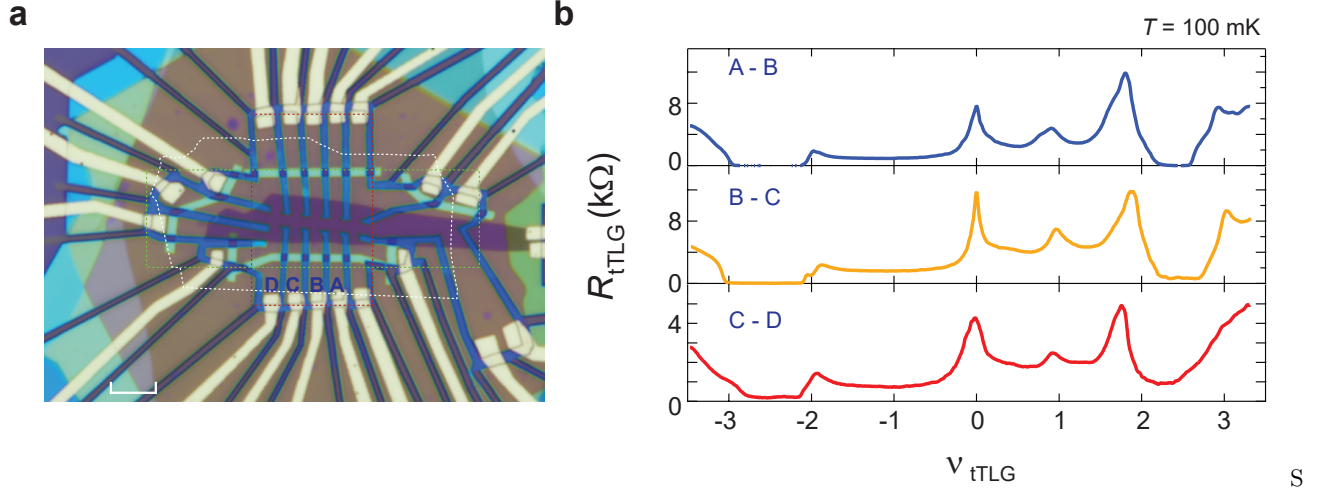


FIG. S1. **The device characterization.** (a) Optical image of the hybrid double-layer device. The red, green and white dashed contours highlight tTLG, Bernal bilayer graphene and the middle 2 nm thick hBN layers, respectively. The hall bar channel is fabricated in the bubble-free region. The scale bar is 5 μm . (b) The four-terminal longitudinal resistance R_{tTLG} obtained from different contact pairs labelled in (a) vs ν_{tTLG} at $T=100$ mK. The measured R_{tTLG} are almost the same among different contact pairs, showing the high uniformity in this device.

II. Transport measurements

The device geometry of the hybrid double-layer structure allows independent control of carrier density in Bernal BLG and tTLG, n_{BLG} and n_{tTLG} , as well as displacement field D . Such control is achieved by applying a DC gate voltage to top graphite electrode V_{top} , bottom graphite electrode V_{bot} , along with a voltage bias between BLG and tTLG V_{int} . n_{BLG} , n_{tTLG} and D can be obtained using the following equations:

$$n_{BLG} = (C_{top}V_{top} + C_{int}V_{int})/e + n_{BLG}^0, \quad (1)$$

$$D_{BLG} = (C_{top}V_{top} - C_{int}V_{int})/2\epsilon_0, \quad (2)$$

$$n_{tTLG} = (C_{bot}V_{bot} + C_{int}V_{int})/e + n_{tTLG}^0, \quad (3)$$

$$D_{tTLG} = (-C_{bot}V_{bot} + C_{int}V_{int})/2\epsilon_0, \quad (4)$$

where C_{top} is the geometric capacitance between top graphite and BLG, C_{bot} the geometric capacitance between bottom graphite and tTLG, and C_{int} the geometric capacitance between BLG and tTLG. n_{BLG}^0 and n_{tTLG}^0 are

intrinsic doping in BLG and tTLG, respectively.

Transport measurement is performed in a BlueFors LD400 dilution refrigerator with a base temperature of 20 mK. Temperature is measured using a resistance thermometer located on the sample probe. We utilize an external multi-stages low-pass filter that is installed on the mixing chamber of the dilution unit [12]. The filter contains two filter banks, one with RC circuits and one with LC circuits. The radio frequency low-pass filter bank (RF) contains three reflective 7-pole Pi filter stages, which are individually shielded and attenuate above 80 MHz; whereas the low frequency low-pass filter bank (RC) contains one reflective 7-pole Pi and two dissipative RC filter stages, which are individually shielded and attenuate from 50 kHz. The filter is commercially available from QDevil.

We performed measurements in different cryostats with the external magnetic field intended to align with the sample plane. Unless otherwise specified, the tilt angle θ in this paper indicates the angle between the device plane and the direction of the applied magnetic field. We use Hall resistance as a function of carrier density near the charge neutrality point to determine the tilt angle. Under a certain external magnetic field B_{total} , according to $R_{xy}^{-1} = ne/B_{\perp}$, the out-of-plane field component B_{\perp} can be extracted by calculating the linear slope of the inverse Hall resistance R_{xy}^{-1} vs carrier density n . The tilt angle θ is then determined by $B_{\perp} = B_{total}\sin\theta$. The first experiment is performed in the BlueFors LD400 system introduced above, where the tilt angle of the sample holder is fixed, resulting in a small tilt angle between the device plane and the applied field of $\sim 2^{\circ}$. For this experiment, the tilt angle is determined to be $\sim 2^{\circ}$ (see FIG. S2(a)). The second experiment is performed in a He3 system with a rotating sample stage at the national high magnetic field lab (SCM-2). We used a single stage low-pass RC filter, which is mounted on the sample probe, to suppress the influence of the RF noises. To eliminate the out-of-plane component in the B -field, we rotate the sample stage at $B_{total} = 15$ T while monitoring Hall resistance near the charge neutrality point (see FIG. S2(b)). The magnitude of R_{xy} near the charge neutrality point is minimized when the tilt angle approach zero. In this experiment, the tilt angle is fixed at zero within the angular resolution that is defined by the minimum step in the mechanical rotation of the sample stage, $\sim 0.1^{\circ}$. We note that, the re-entrant superconducting phase reported by Ref. [19] is not observed in our device. The absence of the re-entrant phase could arise from several different factors: (i) owing to the accuracy of the mechanical rotator, there is always a non-zero, albeit small, out-of-plane magnetic field. It is possible that the re-entrant phase is suppressed by the out-of-plane component of the B -field; (ii) despite the fact that BLG is insulating during the measurement with large in-plane B -field, it still contributes extra Coulomb screening which is capable of influencing the ground state order in tTLG [12]. It is conceivable that the re-entrant phase is suppressed by the extra Coulomb screening from BLG. If this is the case, our observation would provide strong indication that this re-entrant phase originates from an all-electron mechanism. However, it is important to point out that transport behavior of graphene moiré samples often differ from one another owing to sample details such as twist angle distribution and disorder. As such, the absence of re-entrant phase in our measurement cannot be taken as definitive proof of its pairing mechanism, until it is shown by future experiment that the stability of superconductivity anti-correlates with the strength of Coulomb screening.

Standard low frequency lock-in techniques with Stanford Research SR830 and SR860 amplifier are used to measure resistance R_{xx} and R_{xy} , with an excitation current of 1 – 5 nA at a frequency of 17.77 – 43.33 Hz.

To extract the chemical potential of tTLG μ_{tTLG} , we ground the Bernal bilayer graphene and apply interlayer bias V_{int} to twisted trilayer graphene layer. Voltage bias of V_{top} and V_{bot} are applied to the top and bottom gate, respectively. In this configuration, n_{BLG} and n_{tTLG} are expressed as a function of voltage bias and chemical potentials:

$$en_{BLG} = C_{top} \left(V_{top} - \frac{\mu_{BLG}(n_{BLG})}{e} \right) + C_{int} \left(V_{int} + \frac{\mu_{tTLG}(n_{tTLG}) - \mu_{BLG}(n_{BLG})}{e} \right) \quad (5)$$

$$en_{tTLG} = C_{bot} \left(V_{bot} - V_{int} - \frac{\mu_{tTLG}(n_{tTLG})}{e} \right) + C_{int} \left(\frac{\mu_{BLG}(n_{BLG}) - \mu_{tTLG}(n_{tTLG})}{e} - V_{int} \right), \quad (6)$$

where C_{top} , C_{bot} and C_{int} are geometric capacitance per unit area for the top, bottom and thin middle hBN dielectric layer, respectively. At the charge neutrality point of the Bernal bilayer graphene, $n_{BLG}=0$ and $\mu_{BLG}=0$. Eq. (5) is simplified to:

$$\mu_{tTLG} = -eV_{int} - e \frac{C_{top}}{C_{int}} V_{top} \quad (7)$$

$$n_{tTLG} = \frac{C_{bot}V_{bot}}{e} + \frac{C_{bot} + C_{int}}{C_{int}e} C_{top}V_{top} \quad (8)$$

By keeping $V_{top} = 0$, the value of V_{int} at the charge neutrality point of bilayer graphene offers a direct measurement for the chemical potential in tTLG μ_{tTLG} . In addition, we extract density n_{tTLG} by $n_{tTLG} = C_{bot}V_{bot}/e$. When fix V_{top} at a constant and non-zero value, the contribution from V_{top} to the chemical potential μ_{tTLG} is just a constant

shift proportional to V_{top} . Note that, by fixing the top gate V_{top} at different constant value, the extracted chemical potential μ_{tTLG} for a constant density n_{tTLG} corresponds to different displacement field D_{tTLG} .

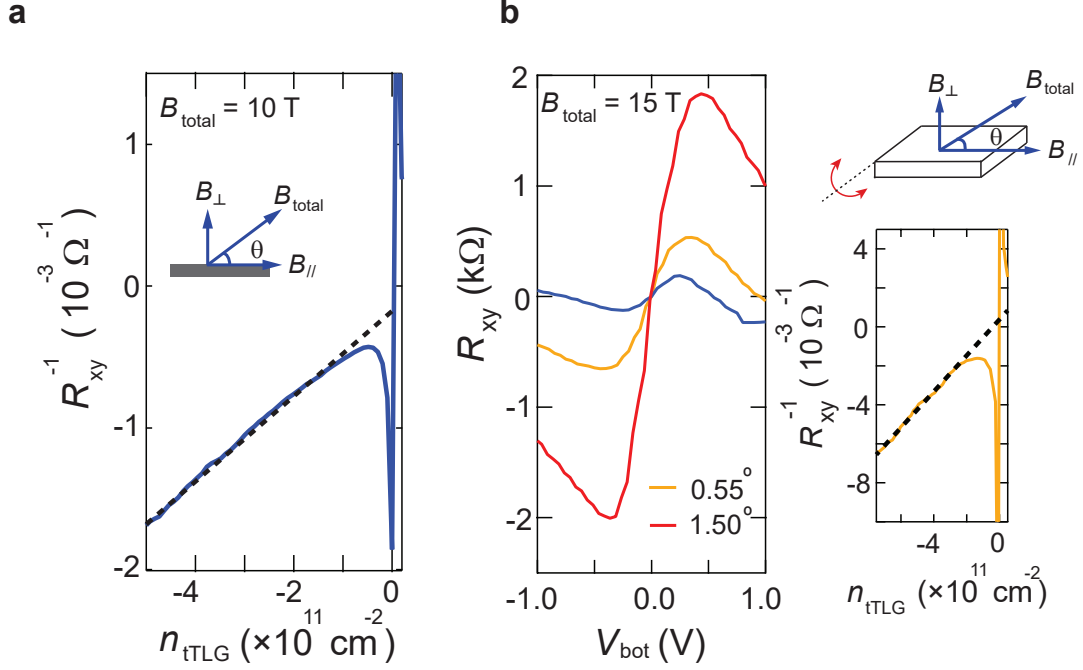


FIG. S2. **Define the tilt angle for the in-plane magnetic field measurements.** (a) Inverse Hall resistance as a function of carrier density n_{tTLG} near the charge neutrality point measured at $B_{total} = 10 \text{ T}$ and $T = 20 \text{ mK}$. According to $R_{xy}^{-1} = ne/B_{\perp}$, by calculating the slope from the linear fitting shown as the dashed line, we obtain $B_{\perp} = 0.35 \text{ T}$, which corresponds to the tilt angle of $\theta = 2^\circ$. (b) Hall resistance R_{xy} versus bottom voltage bias V_{bot} measured with different fixed tilt angles θ at $B_{total} = 15 \text{ T}$ and $T = 300 \text{ mK}$. The right panel shows the inverse Hall resistance vs n_{tTLG} at $\theta = 0.55^\circ$, and the linear fitting is shown as the black dashed line. The tilt angle is calculated as the same method in (a). The blue trace shows R_{xy} measured at the minimum tilt angle. Given the small Hall resistance, variations in R_{xy} are most likely dominated by mixing from the longitudinal channel. This minimum tilt angle in our measurement is regarded as the nominal zero tilt angle, where all the fully in-plane magnetic field dependence measurements are performed.

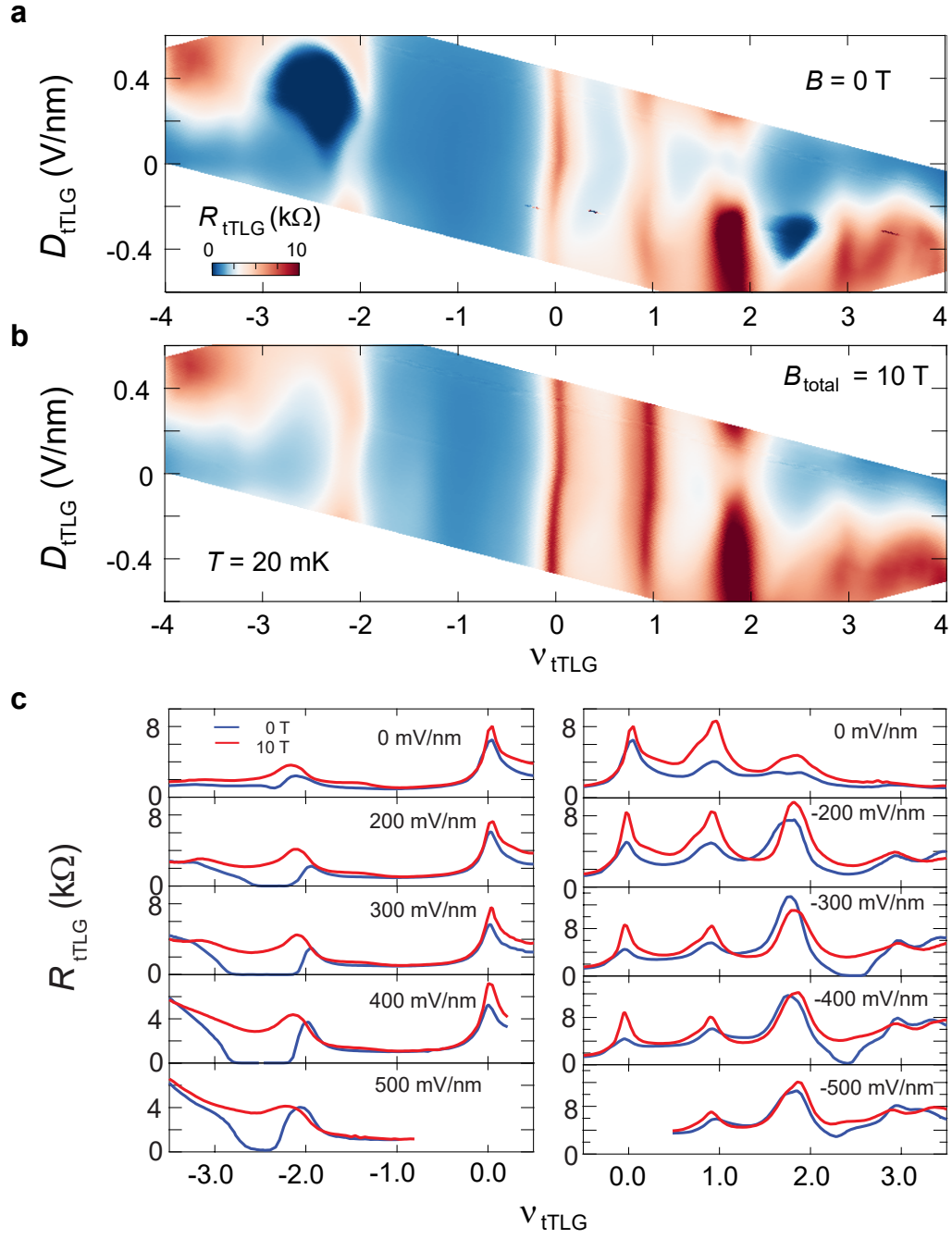


FIG. S3. **The effect of in-plane Zeeman coupling at different D .** The longitudinal resistance R_{tTLG} as a function of V_{tTLG} and D_{tTLG} at (a) $B = 0$ T and (b) total magnetic field $B_{total} = 10$ T measured at $T = 20$ mK. (c) The linecuts of R_{tTLG} vs V_{tTLG} at different total magnetic field B_{total} and D_{tTLG} extracted from (a) and (b). The total magnetic field is oriented at an angle relative to the device plane of $\theta = 2^\circ$.

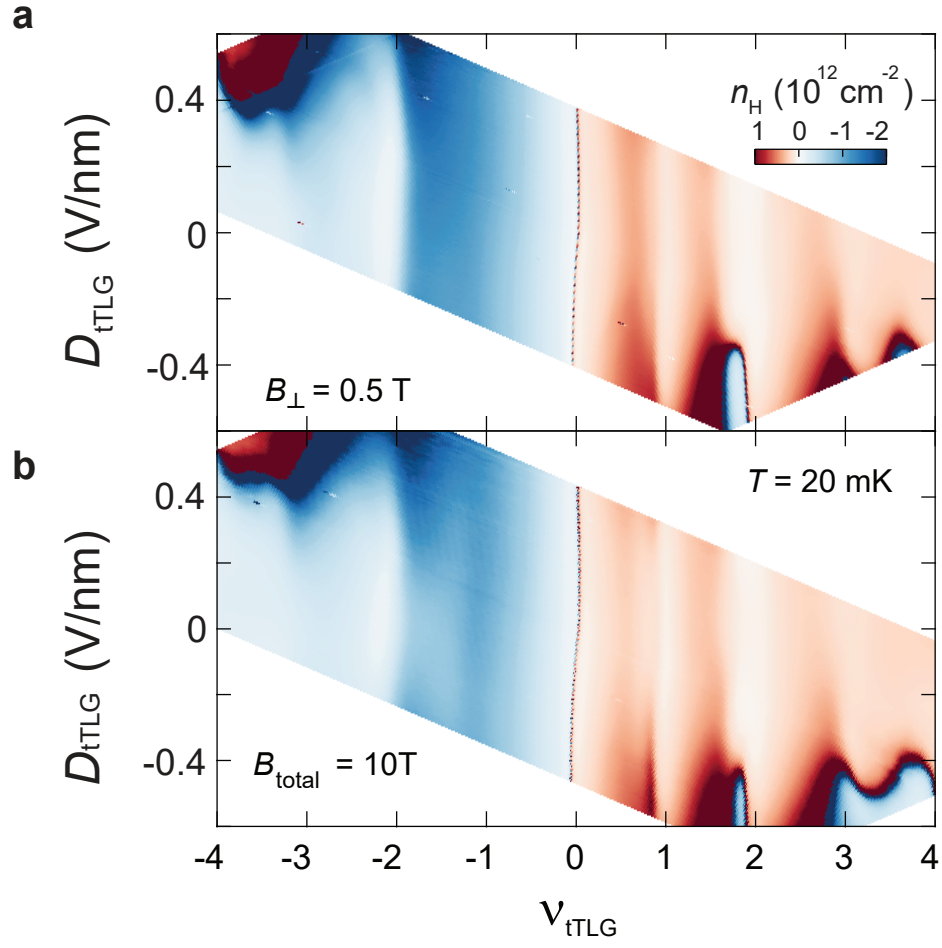


FIG. S4. **Hall density.** (a-b) Hall density n_H as a function of D_{tTLG} and ν_{tTLG} at $T = 20 \text{ mK}$ measured at (a) $B_{\perp} = 0.5 \text{ T}$ and (b) $B_{total} = 10 \text{ T}$ oriented at an angle relative to the device plane of $\theta = 2^\circ$. Isospin-symmetry-breaking transitions, manifested in Hall density resets, remain largely unchanged in the presence of an in-plane B field.

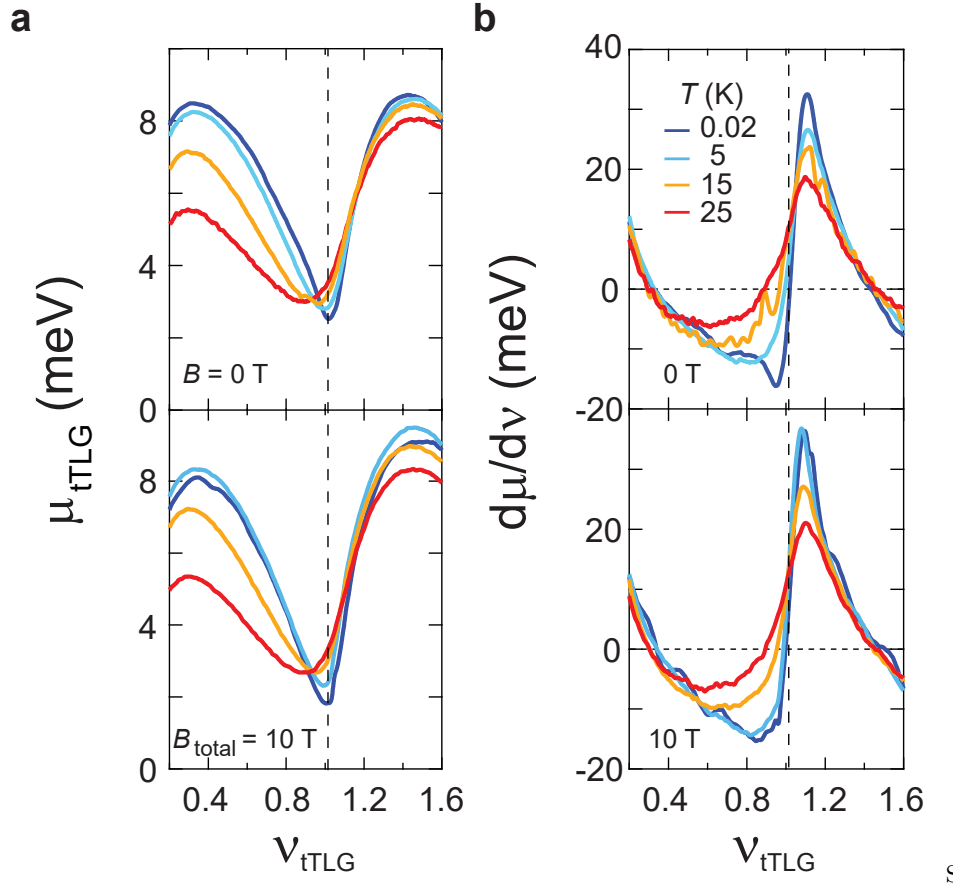


FIG. S5. **Pomeranchuk effect near $\nu = +1$.** (a) Chemical potential μ_{tTLG} and (b) inverse compressibility $d\mu/d\nu$ measured near $\nu_{tTLG} = +1$ at $B = 0$ (top panel) and $B_{total} = 10$ T oriented at an angle relative to the device plane of 2° (bottom panel). The jump in μ_{tTLG} and the sharp peak in $d\mu/d\nu$ denote the Fermi surface reconstruction, which shifts to smaller filling with increasing temperature. At the same time, the position of the same isospin transition appears largely insensitive to in-plane Zeeman coupling. This confirms that the spin degrees of freedom is frozen, owing to large spin stiffness, and the Pomeranchuk transition is driven by fluctuations in valley isospin moment.

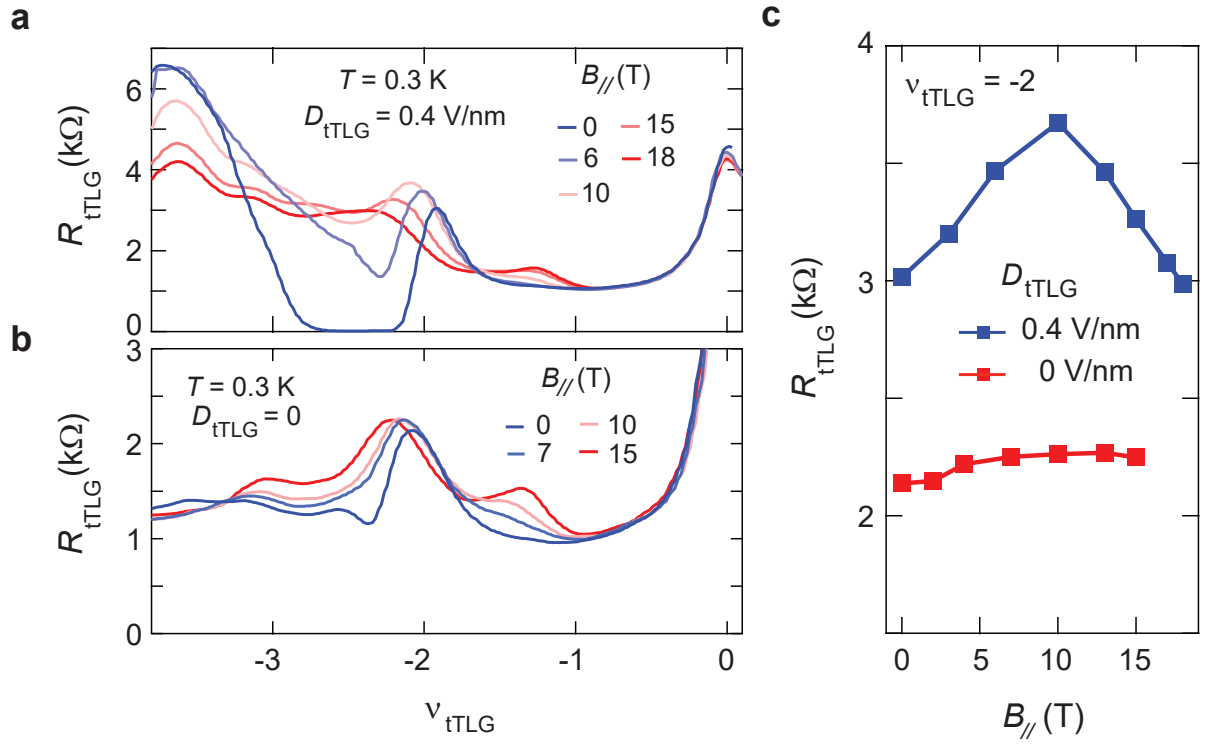


FIG. S6. **The in-plane field dependence of R_{tTLG} at $\nu_{tTLG} = -2$.** R_{tTLG} as a function of ν_{tTLG} at different in-plane magnetic field $B_{||}$ measured at (a) $D_{tTLG} = 400$ mV/nm and (b) $D_{tTLG} = 0$ mV/nm, respectively, and $T = 300$ mK. (c) The value of the resistance peak at $\nu_{tTLG} = -2$ as a function of in-plane magnetic field $B_{||}$ measured at different D_{tTLG} and $T = 300$ mK.

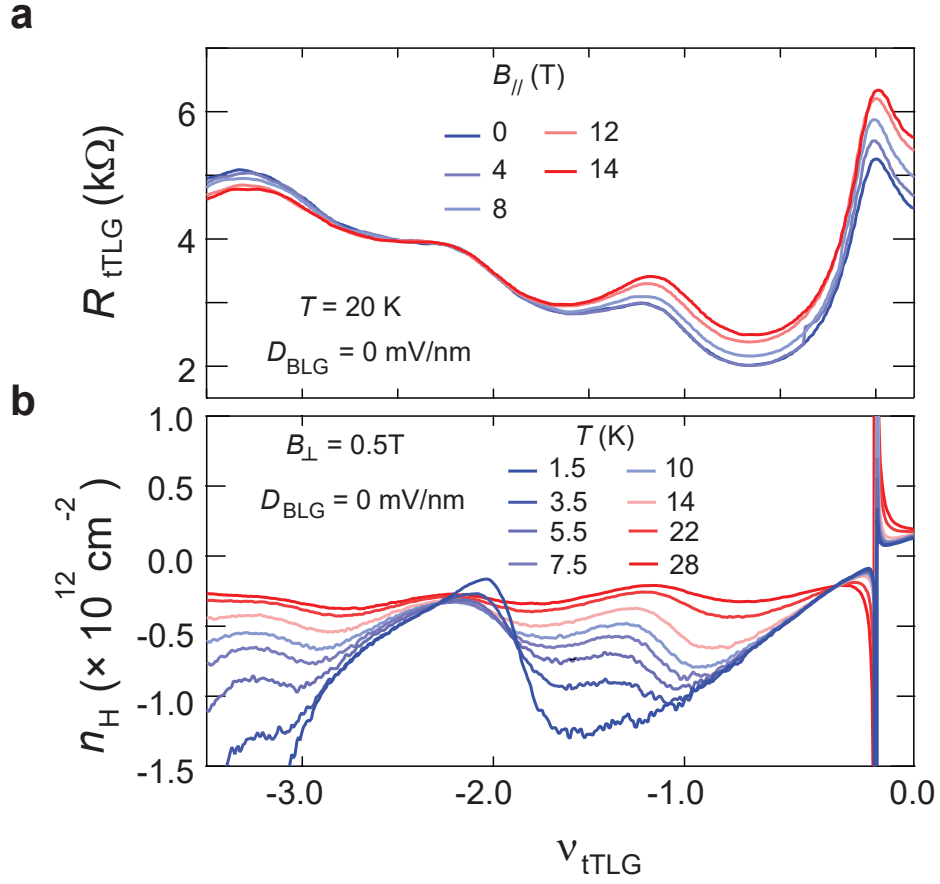


FIG. S7. **Isospin pommeranchuk effect in tTLG.** (a) R_{tTLG} as a function of ν_{tTLG} at different $B_{||}$ measured at $T = 20$ K and $D_{BLG} = 0$ mV/nm. (b) Hall density n_H as a function of ν_{tTLG} at different temperature measured at $B_{\perp} = 0.5$ T and $D_{BLG} = 0$ mV/nm. Near $\nu = -1$, both the position of the resistance peak in (a) and the emerging kink in Hall density at high T in (b) mark the phase boundary between the symmetry-breaking isospin ferromagnet (IF3) and isospin unpolarized state (IU). Such phase boundary is almost unchanged with tuning $B_{||}$ in (a), while shifts to the charge neutrality point apparently with increasing temperature in (b).

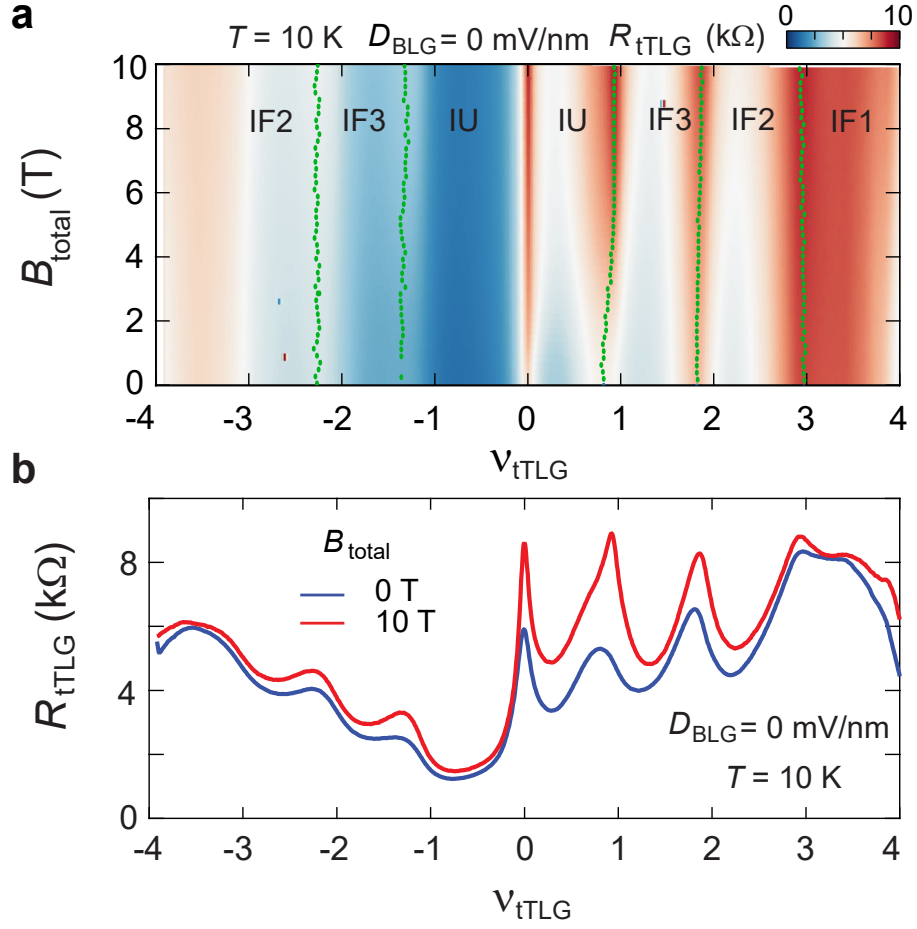


FIG. S8. **The effect of in-plane Zeeman coupling at 10 K.** (a) R_{tTLG} as a function of V_{tTLG} and B_{total} oriented at an angle relative to the device plane θ of 2° measured at $D_{BLG} = 0$ mV/nm and $T = 10$ K. The green dots show the position of R_{tTLG} peak at $\nu = \pm 1, \pm 2$, and $+3$, which denote the boundaries between an isospin unpolarized state IU and the symmetry-breaking isospin ferromagnet IF3, IF2 and IF1. (b) R_{tTLG} versus V_{tTLG} at different B_{total} measured at $D_{BLG} = 0$ mV/nm and $T = 10$ K extracted from (a). The total magnetic field is oriented at an angle relative to the device plane of $\theta = 2^\circ$.

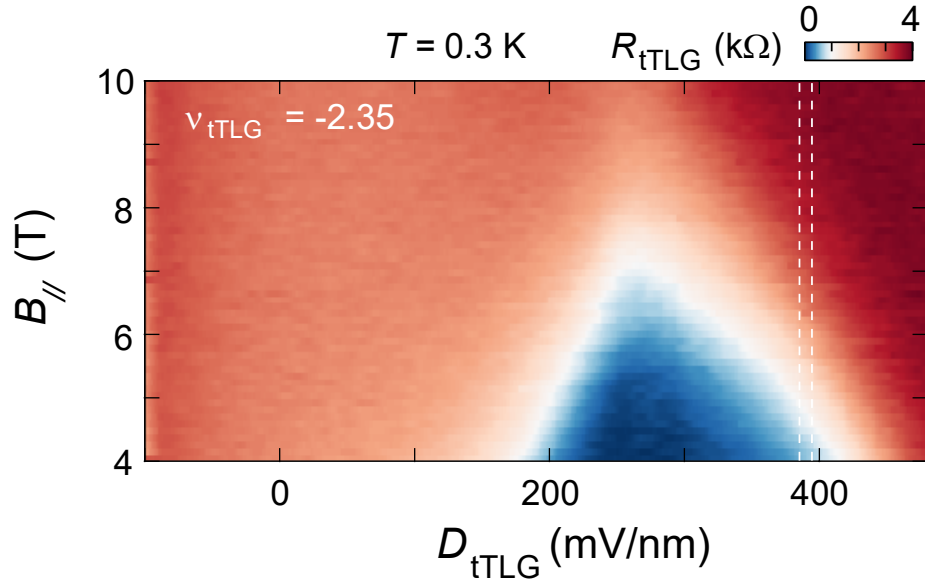


FIG. S9. The D_{tTLG} dependence of superconductivity near $\nu_{tTLG} = -2$ in the Pauli-limit violation regime. R_{tTLG} as a function of D_{tTLG} and $B_{||}$ measured at $\nu_{tTLG} = -2.35$ and $T = 300 \text{ mK}$. The white dashed lines mark the range of D_{tTLG} variation induced by changing n_{BLG} in Fig. 1(i).

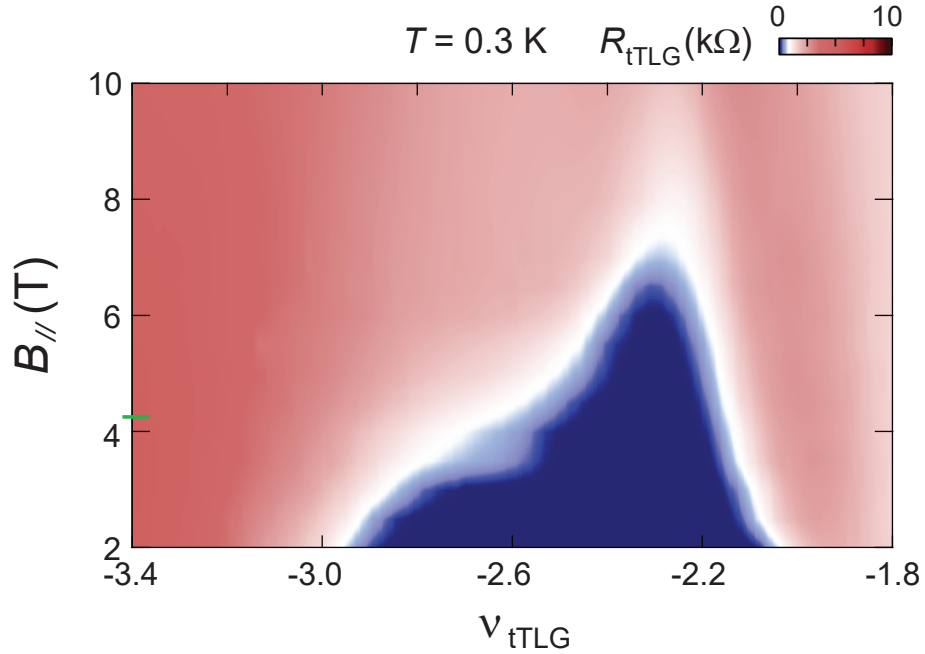


FIG. S10. The in-plane magnetic field dependence of superconductivity near $\nu_{tTLG} = -2$. R_{tTLG} as a function of ν_{tTLG} and $B_{||}$ measured at $T = 300 \text{ mK}$ and $D_{BLG} = 0 \text{ mV/nm}$. The green tick marks the Pauli limit at the optimal doping $B_{||}^{Pauli}$, which is defined by $B_{||}^{Pauli} = 1.86 \text{ (T/K)} \times T_c$, where critical temperature T_c is defined as 50 % of the extrapolated normal state resistance at $B = 0 \text{ T}$.

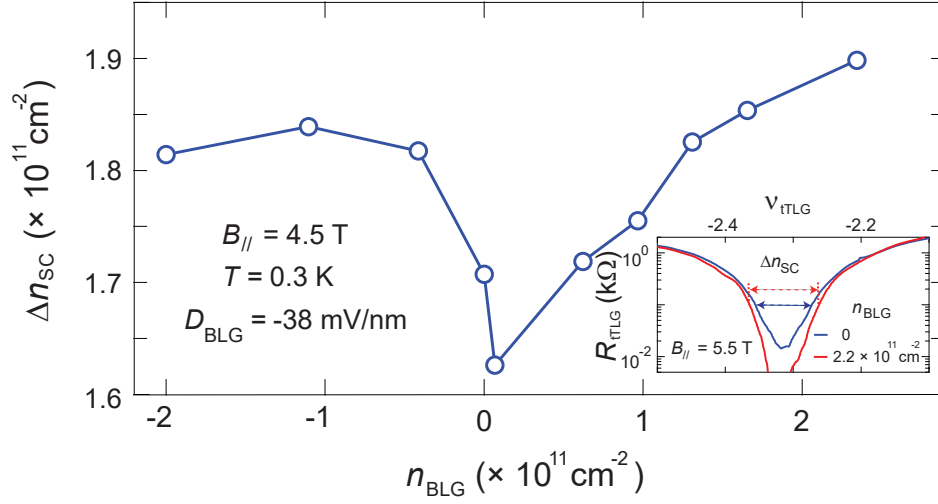


FIG. S11. **The Coulomb screening effect on superconductivity near $\nu_{tTLG} = -2$ in the Pauli limit violation regime.** The density range of superconducting region Δn_{SC} as a function of Bernal density n_{BLG} at $D_{BLG} = -38$ mV/nm measured at $B_{||} = 4.5$ T and $T = 300$ mK. Due to the Pauli limit at the optimal doping $B_{||}^{Pauli}$ is about 4.2 T, this result is measured at $B_{||} > B_{||}^{Pauli}$, where the pauli limit is violated. The inset shows R_{tTLG} vs ν_{tTLG} measured at $D_{BLG} = -38$ mV/nm with different n_{BLG} at $B_{||} = 5.5$ T and $T = 300$ mK. Δn_{SC} is determined by the boundary of the superconducting region, which is practically defined by the density where $R_{tTLG} < 100 \Omega$. At the optimal doping, $D_{BLG} = -38$ mV/nm and $n_{BLG} = 0$ correspond to $D_{tTLG} = 205$ mV/nm for tTLG. Similar to the results in Fig. 1(e), Δn_{SC} in the Pauli limit violation regime is also minimum when Bernal bilayer is fully insulating ($n_{BLG} = 0$).

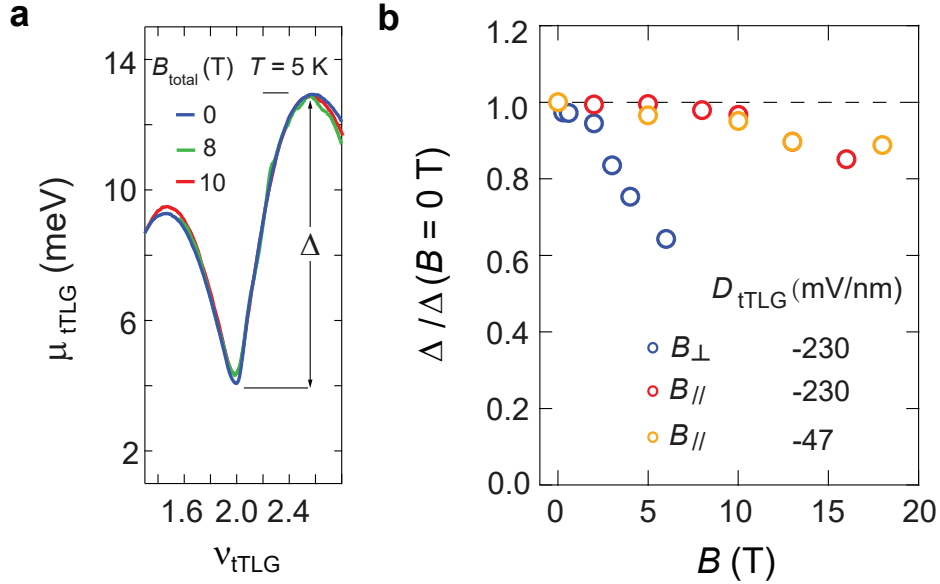


FIG. S12. **The magnetic field dependence of the energy gap at $\nu_{tTLG} = +2$.** (a) Chemical potential μ_{tTLG} measured near $\nu_{tTLG} = +2$ with $D_{tTLG} = -230$ mV/nm at $T = 5$ K and different magnetic fields. μ_{tTLG} at $B_{total} = 8$ T is measured with B aligned fully in-plane, while μ_{tTLG} at $B_{total} = 10$ T is measured with a misalignment of 2° between B and the sample plane, which correspond to $B_{||} = 10$ T and $B_{\perp} = 0.35$ T. The fact that μ_{tTLG} remains the same indicates that the energy gap is not influenced by a small out-of-plane component of B . (b) The same figure as Fig. 2(g). We note that the energy gap at $D_{tTLG} = -230$ mV/nm and $B_{||} = 2$ T, 5 T, 10 T are measured with a 2° misalignment between B and the sample plane, giving rise to an out-of-plane component of 0.35 T. The rest of the data is measured with B aligned fully in-plane. We note that valley index couples to an in-plane magnetic field through a weak orbital effect [39], which could account for the weak $B_{||}$ dependence displayed by $\Delta_{n_s/2}$ and the resistance peak at $B_{||} > 10$ T (Fig. 3g).

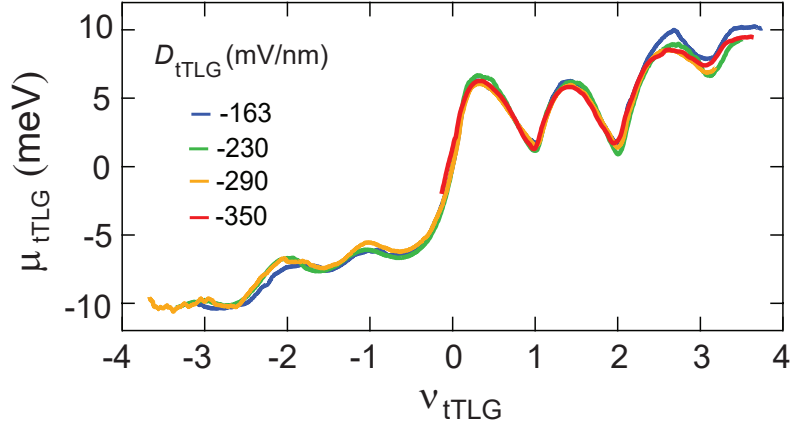


FIG. S13. **Thermodynamic measurement at different D .** Chemical potential μ_{tTLG} as a function of ν_{tTLG} measured at different D_{tTLG} and $T = 20$ mK. The labelled displacement field D_{tTLG} denotes D_{tTLG} at $\nu_{tTLG} = +2$. The chemical potential μ_{tTLG} at different D_{tTLG} are almost overlapped.

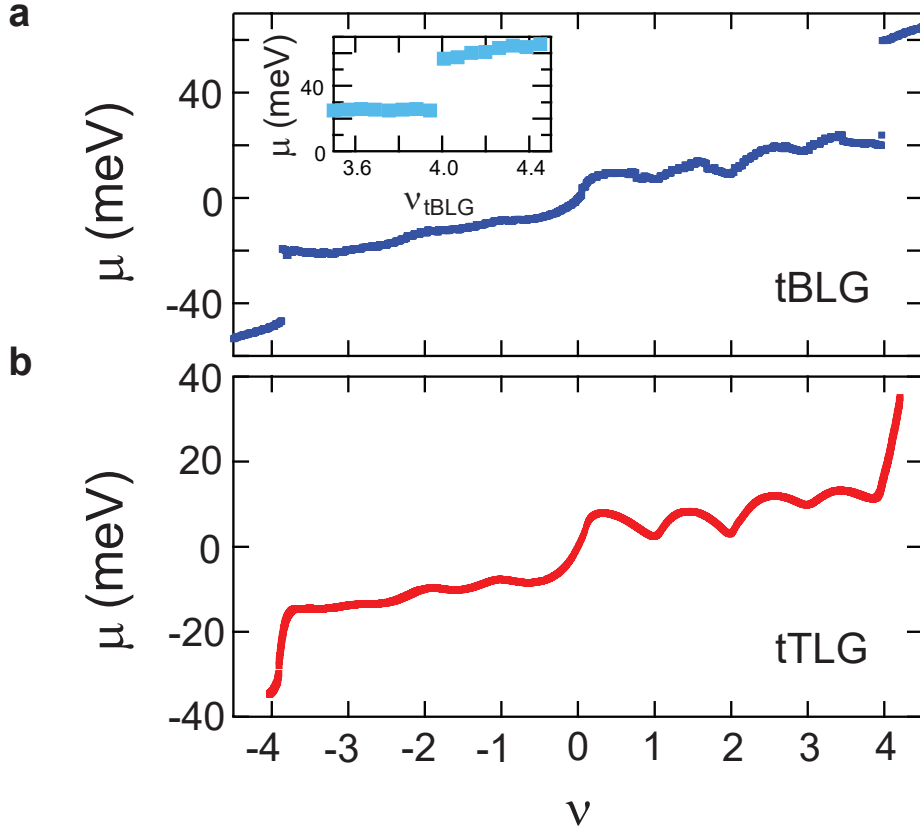


FIG. S14. **The comparison of chemical potential μ measured in MATBG and MATLG.** The chemical potential μ as a function of ν measured in the magic-angle (a) tBLG (the same device studied in [12]) at $T = 20$ mK and (b) tTLG studied in this manuscript at $T = 5$ K, both of which are measured with keeping $V_{top} = 0$ V. The inset in (a) shows chemical potential μ vs ν near $\nu = +4$ measured at $T = 15$ K in the same tBLG device. The chemical potential at $\nu = +/-4$ vary continuously with changing carrier density in tTLG, while it shows the abruptly discontinuous jump in tBLG for both $T = 20$ mK and 15 K. The different slope of chemical potential in tBLG and tTLG varying with density at $\nu = +/-4$ reflects the contribution of the monolayer Dirac band in tTLG.

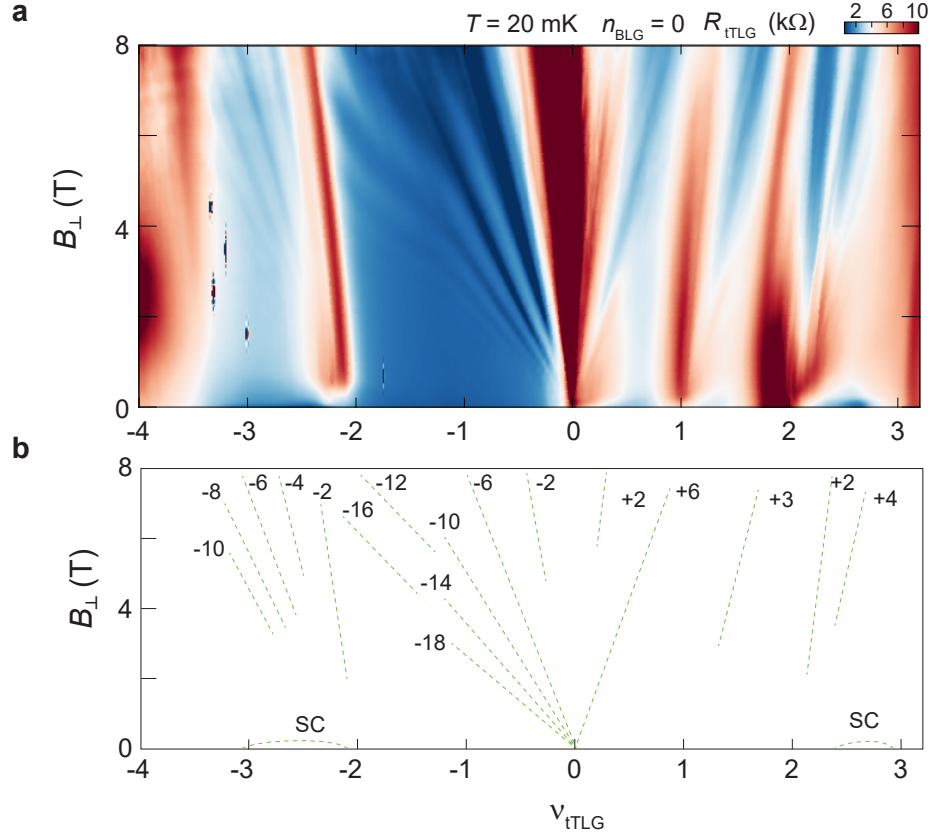


FIG. S15. **Quantum oscillation and Landau fans.** (a) Landau fan diagram of twisted trilayer graphene measured at $D_{BLG} = -50$ mV/nm and $n_{BLG} = 0$ and $T = 20$ mK. (b) Schematic of the Landau fan diagram. The number labels the sequence of quantum oscillations emerging from $\nu_{tTLG} = 0, +1$ and ± 2 , separately.

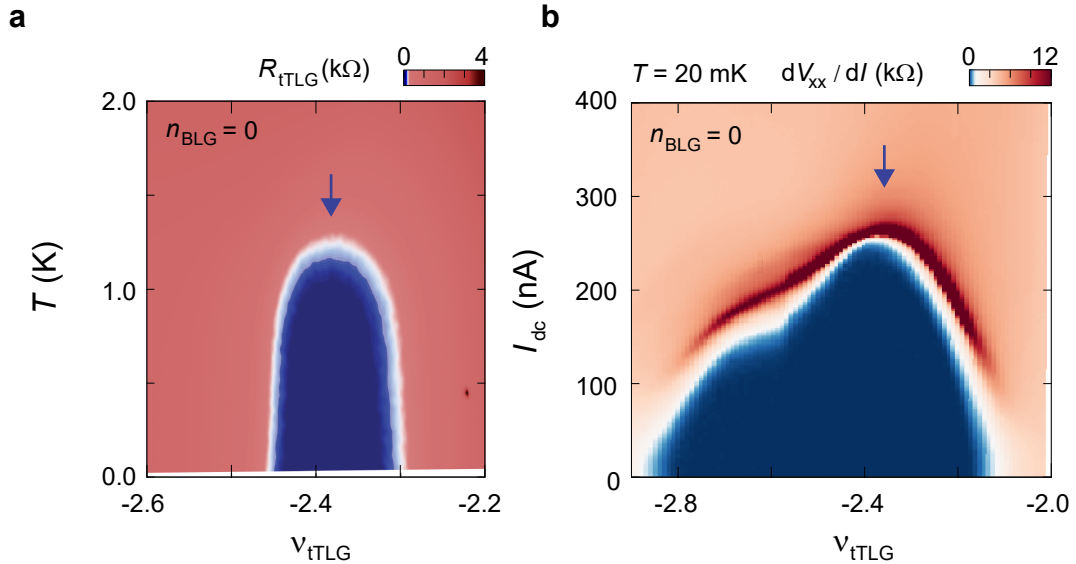


FIG. S16. **Define the optimal doping of superconductivity.** (a) R_{tTLG} vs ν_{tTLG} and T at $D_{BLG} = -163$ mV/nm with $n_{BLG} = 0$. (b) dV_{xx}/dI as a function of ν_{tTLG} and I_{dc} at $D_{BLG} = 125$ mV/nm with $n_{BLG} = 0$ at $T = 20$ mK. The arrows mark the optimal doping of the superconducting dome, where the critical temperature and critical current are maximum. The displacement field D_{tTLG} at the optimal doping are (a) $D_{tTLG} = 95$ mV/nm and (b) $D_{tTLG} = 390$ mV/nm, respectively.

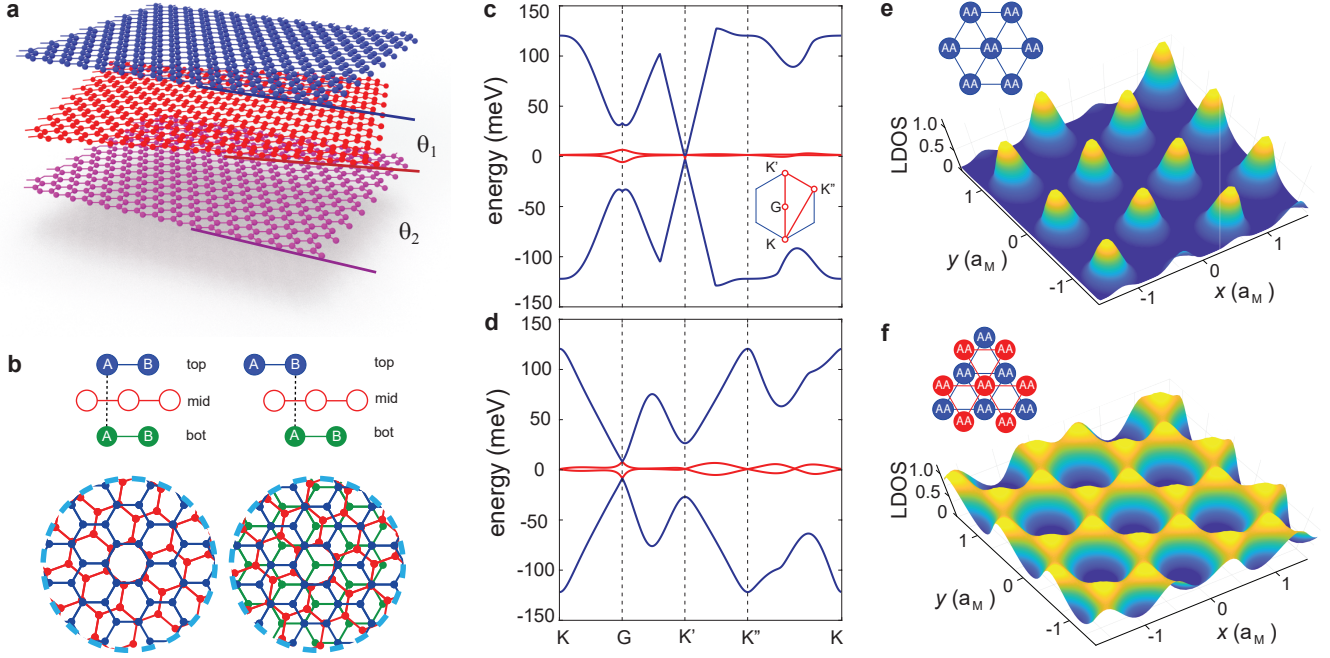


FIG. S17. **The comparison of A-tw-A and A-tw-B stacking order.** (a) schematics of a twisted trilayer graphene structure. θ_1 and θ_2 are twist angles between the top and middle, middle and bottom layers, respectively. (b) top and side views of tTLG with $\theta_1 = \theta_2$ but featuring different stacking orders. Left panel: A-tw-A stacking, the A-sublattice of the top layer is aligned with the A-sublattice of the bottom layer. Right panel: A-tw-B stacking, the B-sublattice of the top layer is aligned with the A-sublattice of the bottom layer. (c-d) calculated band structure for A-tw-A and A-tw-B stacking tTLG near the magic-angle of 1.55 degrees. Both stacking orders feature flat moiré band. (e-f) density distribution of charge carriers in the A-tw-A and A-tw-B stacking tTLG. Charge carriers are concentrated on small islands around the AA sites. These AA sites form a triangular lattice in AA-stacking tTLG, where Wannier function is localized, and Coulomb correlation dominates. In AB-stacking tTLG, AA-sites between top and middle graphene layer are offset from those between the middle and bottom layer (inset in f), thus forming a network with honeycomb lattice. Since electron Wannier function is delocalized in AB-stacking tTLG, we expect Coulomb interaction to play a less prominent role in the ground state order. We thank Yahui Zhang for his input in modeling the band structure and DOS for tTLG with different stacking orders.